Gold-wire Gratings

-for Sensor Applications

Master Thesis

By Jens Christian Uggerhøj
Department of Physics and Nanotechnology, Aalborg University,
Denmark

Department of Physics and Nanotechnology
Skjernvej 4A
DK-9220 Aalborg Øst
Phone: +45 9940 9215
Fax: +45 9940 9235
http://www.nano.aau.dk/

Title:
Gold-wire Gratings
–for Sensor Applications

Project Period:
September, 2010 to October, 2011.

Project Group:
NFM4-5.219B

Attendee:

Jens Christian Uggerhøj

Supervisor:
Kjeld Pedersen

Printrun: 4

Number of Pages: 90

Submitted: October 6, 2011

Abstract

Due to the plasmon resonance conditions of metallic gratings, these can be used for sensor applications. The theoretical aspects of basic plasmonics are investigated and their resonance conditions are reviewed. Through use of Green's function, a theoretical model for the near-field of a gold grating is set up and different parameters are varied in order to investigate the effects on the electrical field around the grating wires.
The experimental work is carried out with focus on producing gold and silicon gratings through e-beam lithography. The structures of the resulting gratings are characterised by use of scanning electron microscopy and atomic force microscopy. The optical properties of the gratings are investigated in terms of second harmonic spectroscopy. The obtained spectra are finally sought explained and related to the theoretical observations.

Institut for fysik og nanoteknologi
Skjernvej 4A
9220 Aalborg Øst
Telefon: +45 9940 9215
Fax: +45 9940 9235
http://www.nano.aau.dk/

Titel:
Gold-wire Gratings
–for Sensor Applications

Projektperiode:
September 2010 til oktober 2011.

Projektgruppe:
NFM4-5.219B

Forfatter:

Jens Christian Uggerhøj

Vejleder:
Kjeld Pedersen

Antal kopier: 4

Antal sider: 90

Afleveret: 6. oktober 2011

Resume

På grund af plasmonresonansbetingelserne kan metalgitre finde anvendelse som sensorer. De teoretiske aspekter vedrørende plasmoner er undersøgt og resonansbetingelserne er gennemgået. En teoretisk model for nærfeltet omkring et guldgitter er opstillet ved brug af Greens funktion og forskellige parametre er varieret for at undersøge effekterne på det elektriske felt omkring gittertrådene.
Det eksperimentelle arbejde er udført med fokus på fremstillingen af guld- og siliciumgitre ved hjælp af e-beam litografi. Strukturerne af de fremstillede gitre er karakteriseret via skannende elektron mikroskopi og atomar kraft mikroskopi. De optiske egenskaber af gitrene er undersøgt med anden harmonisk spektroskopi. Endelig er de resulterende spektre forsøgt forklaret og relateret til teoretiske observationer.

Preface

This report documents a project regarding the making of gold and silicon gratings using e-beam lithography. The report is the product of the ninth and tenth semester project at the Department of Physics and Nanotechnology at Aalborg University during the Fall semester 2010 and Spring semester 2011.

This project is the authors final part of the masters degree in Nanophysics and -materials. Theoretical and technical understanding within the fields of nano-optics and nano-fabrication are the primary goals of this master thesis project.

Structurally, the report is divided into parts, one which covers the theoretical aspects, one which covers the experimental work, and finally a last part containing the conclusive remarks. The report is furthermore divided into chapters and sections; as an example, the notation 3.2 is read Chapter 3 - Section 2. Figures, tables, and equations are designated with two numbers, where the first number denotes the chapter and the second number identifies the figure, table, or equation. In some cases figures are further denoted by a letter e.g. (b), which thus directs the reader to a certain subfigure. All references are denoted e.g. by [4], indicating that the fourth entry in the bibliography is cited.

Contents

1 Introduction

Plasmonics has been of great interest in the recent years. Ultimately, the principles of guiding and modulating surface plasmons are believed to revolutionise the signal processing in connection with optical devices in the future [9]. 'Active' plasmonics has been demonstrated in the sense that e.g. plasmonic waveguides and ring resonators have been produced, cf. e.g. [8; 7; 10]. These conquests have been made possible by the ever improving ability of manufacturing sub wavelength structures where electron-beam lithography and focused-ion-beam lithography are of particular interest since the dimensions of the resulting structures can be controlled very well.
Not only the 'active' plasmonics are of interest—also 'passive' plasmonics have multiple possible uses. An example is the implementation of metallic nano particles into e.g. thin-film solar cells which then functions as scatterers and thus enhances the efficiency of the solar cell. The distinct resonance conditions for the excitation of surface plasmons also make it possible to utilise the phenomenon within the field of sensors. When resonance conditions are fulfilled, a strongly enhanced near-field is formed. This enhanced field couple to the exciting field which thus is strongly scattered or absorbed and a dip is observed in the reflectivity spectrum for the sample. The resonance conditions depend on the surrounding material. Due to the near-field excitations a rather small amount of material adsorbed to the metal surface will change the resonance condition, which will result in increased reflectivity where the dip in reflectivity was previously found—in other words—the surface plasmon is excited at another frequency.
Sensors of this type can be useful for environmental sensing, where the resonance condition is changed due to absorbed target material. Also, for biological sensing applications, the principle is of interest. Here binding assays can be made, which when subjected to a biological sample may bind agent-specific material and thus change the resonance condition.

1.1 Project Overview

During this project, a metallic grating will be produced by use of e-beam lithography. Hands on experience with the techniques used in the production is particularly sought. The grating will be characterised and investigated with respect to some of its optical properties.
The theoretical part of the project will clarify the resonance conditions for the existence of surface plasmons. Further the near-field of a grating will be modelled and investigated.

Theory

I

The theory reviewed in this part first consist of some basic electromagnetism which constitute the foundation for the subsequent chapters.
The conditions for surface plasmon polaritons and localised surface plasmons will be treated. To understand the behaviour of metallic gratings, an integral method will be outlined and applied in order to model the near-field around metallic scatterers.
Finally, some theory about the second harmonic response will be reviewed in order to clarify conditions for possibly observed resonances in the spectra obtained in the experimental part of this project.

Maxwell's Equations

2

When describing the near-field of a scatterer like e.g. a gold wire, a macroscopic approach is taken. This implies that no singular charge or current is considered and that the charge density, ρ and current density, $\vec{j}$ is used instead. The electrodynamic fields related to the problem at hand can be described in terms of Maxwell's equations which are:

$$\begin{aligned}
\nabla \times \vec{E}(\vec{r},t) &= -\frac{\partial \vec{B}(\vec{r},t)}{\partial t}, \\
\nabla \times \vec{H}(\vec{r},t) &= \frac{\partial \vec{D}(\vec{r},t)}{\partial t} + \vec{j}(\vec{r},t), \\
\nabla \cdot \vec{D}(\vec{r},t) &= \rho(\vec{r},t), \\
\nabla \cdot \vec{B}(\vec{r},t) &= 0.
\end{aligned} \tag{2.1}$$

$\vec{E}$ denotes the electric field, $\vec{B}$ the magnetic induction, $\vec{H}$ the magnetic field, and $\vec{D}$ the dielectric displacement. Maxwell's equations were originally introduced to explain the transmission of forces from a source to a receiver—that is—from a source emitting electromagnetic radiation to some structure in which the charges and currents are affected by the electromagnetic radiation. In order to describe the behaviour of matter under the influence of electromagnetic fields, the material's response is related to Maxwell's equations through what is termed the constitutive relations:

$$\begin{aligned}
\vec{D}(\vec{r},t) &= \varepsilon_0 \vec{E}(\vec{r},t) + \vec{P}(\vec{r},t) = \varepsilon_0 \vec{E}(\vec{r},t) + \varepsilon_0 \overleftrightarrow{\chi}_e(\vec{r},t)\vec{E}(\vec{r},t) \equiv \varepsilon_0 \overleftrightarrow{\varepsilon}(\vec{r},t)\vec{E}(\vec{r},t), \\
\vec{B}(\vec{r},t) &= \mu_0 \vec{H}(\vec{r},t) + \mu_0 \vec{M}(\vec{r},t) = \mu_0 \vec{H}(\vec{r},t) + \mu_0 \overleftrightarrow{\chi}_m(\vec{r},t)\vec{H}(\vec{r},t) \equiv \mu_0 \overleftrightarrow{\mu}(\vec{r},t)\vec{H}(\vec{r},t), \\
\vec{j}_c(\vec{r},t) &= \overleftrightarrow{\sigma}(\vec{r},t)\vec{E}(\vec{r},t)
\end{aligned} \tag{2.2}$$

where $\vec{P}$ is the electric polarisation of the material in question, i.e. the response of the material due to the electrical field $\vec{E}$, in terms of a material parameter, $\overleftrightarrow{\chi}_e$ which is termed the electrical susceptibility. $\vec{M}$ is the magnetisation of the material—the magnetic counterpart to the electric polarisation—also related to the material in question through a material dependent parameter, $\overleftrightarrow{\chi}_m$, the magnetic susceptibility. $\overleftrightarrow{\sigma}$ is the conductivity of the media and relates the electrical field to the conduction current density $\vec{j}_c$. The conduction current density constitutes along with the source current density $\vec{j}_s$ the current density $\vec{j}$ (i.e. $\vec{j} = \vec{j}_s + \vec{j}_c$) known from one of Maxwell's equations.

When dealing with Maxwell's equations it is often more convenient to work in the frequency domain instead of the time domain. Through a Fourier representation of the time-dependent equations in (2.1) explicit expressions of the frequency-dependent equations can be obtained. This is done as in the following example,

where Maxwell's curl equation for the electrical field is used:

$$\begin{aligned}
\vec{E}(\vec{r},t) &= \int_{-\infty}^{\infty} \hat{\vec{E}}(\vec{r},\omega)\mathrm{e}^{-i\omega t}\mathrm{d}\omega \Rightarrow \\
\int_{-\infty}^{\infty} \nabla\times\hat{\vec{E}}(\vec{r},\omega)\mathrm{e}^{-i\omega t}\mathrm{d}\omega &= \int_{-\infty}^{\infty} -\frac{\partial}{\partial t}\left(\hat{\vec{B}}(\vec{r},\omega)\mathrm{e}^{-i\omega t}\right)\mathrm{d}\omega \Rightarrow \\
\nabla\times\hat{\vec{E}}(\vec{r},\omega) &= i\omega\hat{\vec{B}}(\vec{r},\omega), \qquad (2.3)
\end{aligned}$$

where the last step taken is valid because of the linearity of the system which implies that the equality in the integral equation must apply to each frequency. The vectors carrying a hat thus denotes the spectrum of the corresponding time-dependent vector without the hat. Maxwell's equations in the frequency domain read:

$$\begin{aligned}
\nabla\times\hat{\vec{E}}(\vec{r},\omega) &= i\omega\hat{\vec{B}}(\vec{r},\omega), \\
\nabla\times\hat{\vec{H}}(\vec{r},\omega) &= -i\omega\hat{\vec{D}}(\vec{r},\omega)+\hat{\vec{j}}(\vec{r},\omega), \\
\nabla\cdot\hat{\vec{D}}(\vec{r},\omega) &= \hat{\rho}(\vec{r},\omega), \\
\nabla\cdot\hat{\vec{B}}(\vec{r},\omega) &= 0. \qquad (2.4)
\end{aligned}$$

From this point and forth, the arguments and hats of the parameters will be understood implicitly and thus omitted—unless they are required for rightful understanding.

3 Plasmonics

Plasmons are typically divided into two groups—surface plasmon polaritons (SPP's) and localised surface plasmons (LSP's).
Surface plasmon polaritons are excitations of the free electrons in the surface of a metal. The plasmon polaritons form as an impinging electromagnetic field couple to the oscillations of the electrons. The resulting waves are not confined along the surface and are termed surface waves. These surface waves are—as opposed to localised surface plasmons—thus able to propagate at the interface between the metal and a dielectric. The surface waves are, however, confined in the perpendicular direction in the sense that the waves decay evanescently into both the metal and the dielectric.
Localised surface plasmons are excitations of the conduction electrons in metallic nanostructures which couple to the electromagnetic field. These occurring resonances lead to field amplification in the near-field zone of the structure in question. The two kinds of plasmons will be reviewed in the following.

3.1 Surface Plasmon Polaritons

When looking for a mathematical description of a surface plasmon polariton, the electrical field must obey the Helmholtz equation:

$$\nabla^2\vec{E}(\vec{r}) + k_0^2\varepsilon(\vec{r})\vec{E}(\vec{r}) = 0, \tag{3.1}$$

where $\vec{k}_0$ is the wave vector in vacuum. A simple waveguide geometry (cf. Figure 3.1) is used in order to more easily illustrate the concept as the problem is greatly simplified this way. The geometry consists of a conductor surrounded by a vacuum. The surface wave is assumed to propagate along the x-direction only and the top surface of the slate is the interface which sustains the surface plasmon polariton. The electrical field can thus be described as $\vec{E}(\vec{r}) = \vec{E}(z)e^{i\beta x}$ where β is the propagation constant of the surface wave. The propagation constant is due to the choice of geometry equal to the x-component of the wave vector, $\vec{k}_0$. Inserting this field into the Helmholtz equation (Equation (3.1)) yields:

$$\begin{aligned}\vec{E}(z)e^{i\beta x}(-\beta^2) + \frac{\partial^2}{\partial z^2}\left(\vec{E}(z)e^{i\beta x}\right) + k_0^2\varepsilon(\vec{r})\vec{E}(\vec{r}) = 0 \Rightarrow \\ \frac{\partial^2\vec{E}(\vec{r})}{\partial z^2} + \left(k_0^2\varepsilon(\vec{r}) - \beta^2\right)\vec{E}(\vec{r}) = 0.\end{aligned} \tag{3.2}$$

Next, the wave equation must be expressed in order to describe the surface plasmon polariton. Before this can be done, explicit expressions for the electrical field components and the corresponding magnetic field components must be found. For this

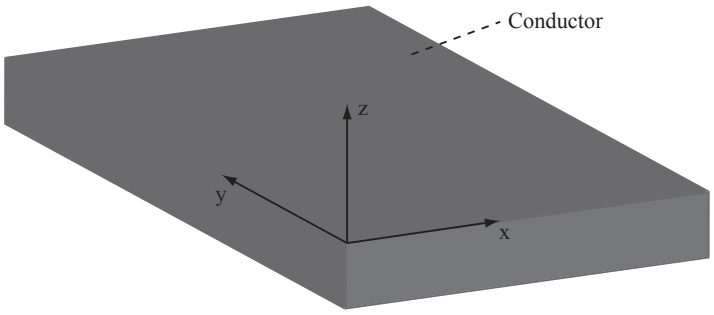

Figure 3.1: Simple planar waveguide geometry.

purpose Maxwell's curl equations are applied. The media is assumed non-magnetic and thus $\vec{B} = \mu_0 \vec{H}$. Furthermore, a harmonic time dependence is assumed and thus the first curl equation yields:

$$\begin{aligned} i\omega\mu_0 \begin{bmatrix} H_x \\ H_y \\ H_z \end{bmatrix} &= \begin{vmatrix} \hat{x} & \hat{y} & \hat{z} \\ \frac{\partial}{\partial x} & \frac{\partial}{\partial y} & \frac{\partial}{\partial z} \\ E_x & E_y & E_z \end{vmatrix} \\ &= \left(\frac{\partial E_z}{\partial y} - \frac{\partial E_y}{\partial z}\right)\hat{x} + \left(\frac{\partial E_x}{\partial z} - \frac{\partial E_z}{\partial x}\right)\hat{y} + \left(\frac{\partial E_y}{\partial x} - \frac{\partial E_x}{\partial y}\right)\hat{z}. \end{aligned} \tag{3.3}$$

It is also assumed that no external current exists and with $\vec{D} = \varepsilon_0 \varepsilon \vec{E}$ the second curl equation yields:

$$\begin{aligned} -i\omega\varepsilon_0\varepsilon \begin{bmatrix} E_x \\ E_y \\ E_z \end{bmatrix} &= \begin{vmatrix} \hat{x} & \hat{y} & \hat{z} \\ \frac{\partial}{\partial x} & \frac{\partial}{\partial y} & \frac{\partial}{\partial z} \\ H_x & H_y & H_z \end{vmatrix} \\ &= \left(\frac{\partial H_z}{\partial y} - \frac{\partial H_y}{\partial z}\right)\hat{x} + \left(\frac{\partial H_x}{\partial z} - \frac{\partial H_z}{\partial x}\right)\hat{y} + \left(\frac{\partial H_y}{\partial x} - \frac{\partial H_x}{\partial y}\right)\hat{z}. \end{aligned} \tag{3.4}$$

Because of the assumptions made in connection with the geometric setup, the partial derivative with respect to the x-direction is proportional to the propagation constant, i.e. $\frac{\partial}{\partial x} \Rightarrow i\beta$. Furthermore, the derivative with respect to the y-direction is zero. The equations then simplify to:

$$\begin{aligned} i\omega\mu_0 H_x &= -\frac{\partial E_y}{\partial z} \\ i\omega\mu_0 H_y &= \frac{\partial E_x}{\partial z} - i\beta E_z \\ i\omega\mu_0 H_Z &= i\beta E_y \end{aligned}$$

$$\begin{aligned} -i\omega\varepsilon_0\varepsilon E_x &= -\frac{\partial H_y}{\partial z} \\ -i\omega\varepsilon_0\varepsilon E_y &= \frac{\partial H_x}{\partial z} - i\beta H_z \\ -i\omega\varepsilon_0\varepsilon E_z &= i\beta H_y. \end{aligned} \tag{3.5}$$

The number of equations can be reduced further if only certain polarisations are treated. In this context two on each other orthogonal polarisations are observed—namely the *p*-polarised electric field which is polarised parallel to the plane of incidence and the *s*-polarised electric field which thus inherently is polarised perpendicular to the plane of incidence. For the *p*-polarised case, the *y*-component of the electrical field along with the *z*-component of the magnetic field are both zero. From this, it follows that also the *x*-component of the magnetic field is zero. The fourth and sixth entry in Equation (3.5) yield the non-zero electric field components in terms of the *y*-component of the corresponding magnetic field:

$$\begin{aligned} E_x &= -i\frac{1}{\omega\varepsilon_0\varepsilon}\frac{\partial H_y}{\partial z} \\ E_z &= -\frac{\beta}{\omega\varepsilon_0\varepsilon}H_y. \end{aligned} \tag{3.6}$$

Inserting these into the second entry of Equation (3.5) yields the wave equation for the *p*-polarised mode:

$$\frac{\partial^2 H_y}{\partial z^2} + \left(k_0^2\varepsilon - \beta^2\right) H_y = 0. \tag{3.7}$$

Similar for the *s*-polarised case, the *z*-component of the electric field and the *y*-component of the magnetic field are both zero. Correspondingly the *x*-component of the electric field turns out to be zero and the magnetic components of the *s*-polarised electric field are:

$$\begin{aligned} H_x &= i\frac{1}{\omega\mu_0}\frac{\partial E_y}{\partial z} \\ H_z &= \frac{\beta}{\omega\mu_0}E_y. \end{aligned} \tag{3.8}$$

While the wave equation governing the *s*-polarised mode becomes:

$$\frac{\partial^2 E_y}{\partial z^2} + \left(k_0^2\varepsilon - \beta^2\right) E_y = 0. \tag{3.9}$$

Starting with the *s*-polarised mode and looking for solutions to the wave equation (Equation (3.9)) that decay into the vacuum (i.e. for $z > 0$), the electric field, E_y, along with the magnetic field components from Equation (3.8) are:

$$E_{y_2} = A_2 \mathrm{e}^{-k_{z_2} z} \mathrm{e}^{i\beta x} \tag{3.10}$$

$$H_{x_2} = -iA_2 k_{z_2} \frac{1}{\omega\mu_0} \mathrm{e}^{-k_{z_2} z} \mathrm{e}^{i\beta x} \tag{3.11}$$

$$H_{z_2} = A_2 \frac{\beta}{\omega\mu_0} \mathrm{e}^{-k_{z_2} z} \mathrm{e}^{i\beta x}. \tag{3.12}$$

Similar for the solution which decays into the metal (for $z < 0$):

$$E_{y_1} = A_1 e^{k_{z_1} z} e^{i\beta x} \tag{3.13}$$

$$H_{x_1} = iA_1 k_{z_1} \frac{1}{\omega\mu_0} e^{k_{z_1} z} e^{i\beta x} \tag{3.14}$$

$$H_{z_1} = A_1 \frac{\beta}{\omega\mu_0} e^{k_{z_1} z} e^{i\beta x}. \tag{3.15}$$

In order to match the solutions across the interface ($z = 0$) continuity is required. That is—$E_{y_1} = E_{y_2}$ and $H_{x_1} = H_{x_2}$. From matching the y-components of the electrical fields it is found that $A_1 = A_2$. When matching the x-components of the magnetic fields a certain condition arises, namely $A_1(k_{z_1} + k_{z_2}) = 0$. Through the notation used so far, the real part of both k_{z_1} and k_{z_2} are required to be positive. If the above condition must apply, then it is evident that A_1 must equal zero, which means that no surface plasmon polariton exists for s-polarised instances.
Continuing with the p-polarised mode and looking for solutions in the same way as for the s-polarised mode, the following sets of equations apply. For $z > 0$, the magnetic field, H_y, is:

$$H_{y_2} = A_2 e^{-k_{z_2} z} e^{i\beta x}. \tag{3.16}$$

From this and Equation (3.6), the electric field components follows:

$$E_{x_2} = iA_2 k_{z_2} \frac{1}{\omega\varepsilon_0\varepsilon_2} e^{-k_{z_2} z} e^{i\beta x} \tag{3.17}$$

$$E_{z_2} = -A_2 \frac{\beta}{\omega\varepsilon_0\varepsilon_2} e^{-k_{z_2} z} e^{i\beta x}. \tag{3.18}$$

And for the solution which decays into the metal ($z < 0$):

$$H_{y_1} = A_1 e^{k_{z_1} z} e^{i\beta x} \tag{3.19}$$

$$E_{x_1} = -iA_1 k_{z_1} \frac{1}{\omega\varepsilon_0\varepsilon_1} e^{k_{z_1} z} e^{i\beta x} \tag{3.20}$$

$$E_{z_1} = -A_1 \frac{\beta}{\omega\varepsilon_0\varepsilon_1} e^{k_{z_1} z} e^{i\beta x}. \tag{3.21}$$

Next step is to invoke boundary conditions at the interface ($z = 0$). Continuity of the normal component of the dielectric displacement field $D_{z_1} = D_{z_2}$ requires that:

$$\begin{aligned} \varepsilon_1 E_{z_1} &= \varepsilon_2 E_{z_2} \Rightarrow \\ -\varepsilon_1 A_1 \frac{\beta}{\omega\varepsilon_0\varepsilon_1} e^{i\beta x} &= -\varepsilon_2 A_2 \frac{\beta}{\omega\varepsilon_0\varepsilon_2} e^{i\beta x} \Rightarrow \\ A_1 &= A_2. \end{aligned} \tag{3.22}$$

Furthermore, continuity of the tangential component of the electrical field is required. This condition is fulfilled when:

$$\begin{aligned} E_{x_1} &= E_{x_2} \Rightarrow \\ -iA_1 k_{z_1} \frac{1}{\omega\varepsilon_0\varepsilon_1} e^{i\beta x} &= iA_2 k_{z_2} \frac{1}{\omega\varepsilon_0\varepsilon_2} e^{i\beta x} \Rightarrow \\ \frac{k_{z_2}}{k_{z_1}} &= -\frac{\varepsilon_2}{\varepsilon_1}. \end{aligned} \tag{3.23}$$

From the wave equations in both half-spaces it also follows that $k_{z_1}^2 + k_0^2\varepsilon_1 - \beta^2 = 0$ and $k_{z_2}^2 + k_0^2\varepsilon_2 - \beta^2 = 0$. Combining these with Equation (3.23) yields:

$$\begin{aligned}
\frac{k_{z_2}^2}{k_{z_1}^2} &= \frac{\beta^2 - k_0^2\varepsilon_2}{\beta^2 - k_0^2\varepsilon_1} = \frac{\varepsilon_2^2}{\varepsilon_1^2} \Rightarrow \\
\left(\beta^2 - k_0^2\varepsilon_2\right)\varepsilon_1^2 &= \left(\beta^2 - k_0^2\varepsilon_1\right)\varepsilon_2^2 \Rightarrow \\
\beta^2\left(\varepsilon_1^2 - \varepsilon_2^2\right) &= k_0^2\varepsilon_1\varepsilon_2\left(\varepsilon_1 - \varepsilon_2\right) \Rightarrow \\
\beta^2 &= k_0^2\frac{\varepsilon_1\varepsilon_2\left(\varepsilon_1 - \varepsilon_2\right)}{\left(\varepsilon_1 + \varepsilon_2\right)\left(\varepsilon_1 - \varepsilon_2\right)} \Rightarrow \\
\beta &= k_0\sqrt{\frac{\varepsilon_1\varepsilon_2}{\varepsilon_1 + \varepsilon_2}},
\end{aligned} \tag{3.24}$$

which is the dispersion relation for the surface plasmon polariton. If one of the z-components of the wave vector is isolated instead, further restrictions to the electric constants and thus the choice of materials can be found:

$$\begin{aligned}
k_{z_1}^2 + k_0^2\varepsilon_1 - \beta^2 &= k_{z_2}^2 + k_0^2\varepsilon_2 - \beta^2 \Rightarrow \\
k_{z_1}^2 &= \frac{\varepsilon_2^2}{\varepsilon_1^2}k_{z_1}^2 + k_0^2\left(\varepsilon_2 - \varepsilon_1\right) \Rightarrow \\
k_{z_1}^2\left(1 - \frac{\varepsilon_2^2}{\varepsilon_1^2}\right) &= k_0^2\left(\varepsilon_2 - \varepsilon_1\right) \Rightarrow \\
k_{z_1}^2\frac{\left(\varepsilon_1 + \varepsilon_2\right)\left(\varepsilon_1 - \varepsilon_2\right)}{\varepsilon_1^2} &= k_0^2\left(\varepsilon_2 - \varepsilon_1\right) \Rightarrow \\
k_{z_1} &= k_0\sqrt{\frac{-\varepsilon_1^2}{\varepsilon_1 + \varepsilon_2}}.
\end{aligned} \tag{3.25}$$

In order for k_{z_1} to be real as required, the denominator $(\varepsilon_1 + \varepsilon_2)$ of Equation (3.25) should be negative. Potentially both materials could have a negative dielectric constant and the expression would still be fulfilled. However, if it is held up against the surface plasmon dispersion relation, where it is required that also β should be real it is seen that the product of the dielectric constants should be negative, which implies that one—and only one—of the materials is required to be a conductor.

The dispersion relation for a metal described through the Drude model is plotted in Figure 3.2. To the left of the light line, the allowed modes arise for frequencies above the plasma frequency. These modes are not bound and are termed radiative modes as they occur in the transparency regime of the conductor and thus radiates into the metal. The imaginary modes occurring in between the real modes constitute a frequency gap where propagation is prohibited. The real modes to the right of the light line represent the bound surface modes. Due to the fact that the modes lie away from the light line, there is a wave vector mismatch which has to be compensated for if a surface plasmon polariton has to be excited. Different techniques such as grating coupling or phenomena such as enhanced near fields can yield the required change in wave vector.

In real metals, with attenuation taken into account, the dispersion relation is slightly

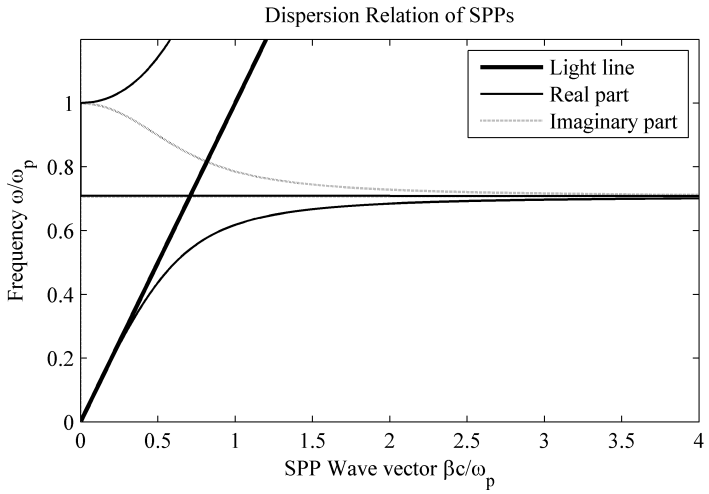

Figure 3.2: SPP dispersion relation for a Drude metal ($\varepsilon = 1 - \frac{\omega_p^2}{\omega^2}$) combined with a vacuum ($\varepsilon = 1$). The metal is assumed to be without attenuation and the plasma frequency is set to $\omega_p = 3 \cdot 10^{15}\ s^{-1}$.

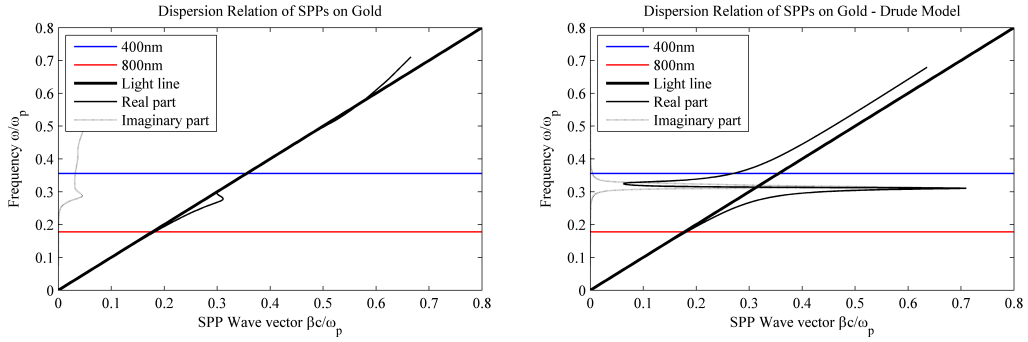

(a) (b)

Figure 3.3: (a) SPP dispersion relation for gold surrounded by a vacuum. The dielectric constant for gold has been calculated by use of the refractive index data from [12]. (b) Drude model ($\varepsilon = \varepsilon_{interband} - \frac{\omega_p^2}{\omega(\omega + i\gamma)}$) of gold has been used to image the SPP dispersion relation. The parameters $\varepsilon_{interband} = 9.25$, $\omega_p = 1.325 \cdot 10^{16}\ s^{-1}$, and $\gamma = 5.850 \cdot 10^{13}\ s^{-1}$ have been found by fitting them to the data from [12]. The obtained fit of ω_p from the Drude model has been used for normalisation in both cases.

different. In Figures 3.3(a) and (b) are dispersion relations for gold depicted. It is seen that the implementation of damping to the Drude model and the use of true dielectric constant data closes the frequency gap experienced in the case of an ideal conductor. Furthermore, it is seen that the dispersion constant, β of the bound states no longer approaches infinity, but that now there is actually a maximum wave vector belonging to the system. Close to this maximum wave vector, the surface plasmons are confined the most. The surface plasmons also exhibit a rather poor propagation length close to this frequency. This phenomenon concerning a trade-off between confinement to the surface and propagation length is a characteristic problem when dealing with SPP's [10]. This is illustrated in Figure 3.4(a), where the penetration depth and propagation length of surface plasmons have been plotted. The propaga-

tion length is defined as the length where the intensity of the surface plasmon has dropped to $1/\mathrm{e}$ of the maximum. As the field of the SPP is proportional to $e^{i\beta x}$ and the intensity thus is proportional to the expression squared, the propagation length is found as $L = \frac{1}{2Im[\beta]}$. The penetration depths are defined in the same way and are found by $z_i = \frac{1}{2Re[k_{z_i}]}$ where $k_{z_i} = \sqrt{\beta^2 - \varepsilon_i k_0^2}$. It is seen that the poorer the confine-

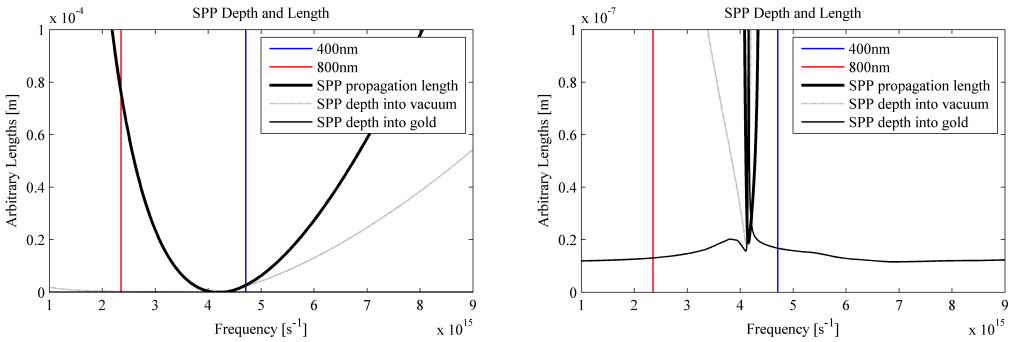

(a) (b)

Figure 3.4: (a) SPP propagation length and penetration depth in the case of gold surrounded by a vacuum. The SPP propagation constants were found by use of a Drude model with parameters resembling gold. (b) Zoom-in of Figure (a), where the penetration depth into the gold half-space now is observable.

ment to the surface, the longer the propagation length of the SPP. Furthermore, the penetration depth into the gold is seen to be rather small—less than 20 nm across most of the frequency range.

As before mentioned a wave vector mismatch exists and in order to excite a surface plasmon this mismatch has to be compensated for—that is—the propagation constant must equal the sum of the wave vector of the impinging electromagnetic field and some other momentum component, $\beta = k\sin(\theta) \pm \delta k_x$, where θ is the angle of incidence of the exciting electromagnetic field and $\vec{k}$ is the wave vector in the dielectric media. Different approaches exist for the addition of the required momentum components. Simple surface roughness can function as scatterers where different momenta can be obtained. Similar can an enhanced near-field yield the required change in momentum. These conditions are not necessarily well-controlled and specific waveguides responding to certain frequencies cannot easily be tailored. If a certain momentum component is wanted, one can manufacture suitable scatterers. This can be done by patterning the surface of the conductor with a one-dimensional grating. The phase-matching condition is fulfilled when $\beta = k\sin(\theta) \pm mg$, where $g = \frac{2\pi}{a}$ is the reciprocal grating vector of a grating with a period equal to a, and $m = (1, 2, 3, ...)$. If the grooves become to deep, $> 20\ nm$, the grating can no longer be thought of as a small perturbation of the surface and band gaps do in fact evolve [10]. If the groove depths become even larger again, localised modes within the grooves can be formed which may enable (potentially unwanted) coupling to the exciting electromagnetic field [10].

3.2 Localised Surface Plasmons

The second type of plasmonics is localised surface plasmons. While surface plasmon polaritons are propagating waves coupled to the electrons of a conductor, localised surface plasmons are non-propagating modes of the coupling between an electromagnetic field and the confined electrons of metallic nanostructures. These modes arise in sub-wavelength structures if a resonance condition suiting the exciting electromagnetic field exists. Contrary to surface plasmon polaritons, localised surface plasmons can be excited by direct illumination—no momentum compensation has to be employed.
These resonance conditions for the excitation of LSP's can be found through an electrostatic approach treating metallic spheres. The fact that the problem is treated electrostatically implies that the particles of interest are on the order of 50 nm or smaller in size [6]. For other geometries—other approaches must be taken. If the particle of interest retain some cylindrical geometry—e.g. a spheroid—the electrostatic method in e.g. [14] can be utilised to obtain the resonance conditions. In the 'simple' case of a sphere the resonance condition is [6; 10; 11]:

$$\frac{1}{\varepsilon_1(\omega)+2\varepsilon_2}, \tag{3.26}$$

where ε_1 is the dielectric constant of the sphere and ε_2 is the dielectric constant of the surrounding material. A resonance condition is thus obtained when the denominator approaches zero, which yield the requirement that one of the materials has to be a conductor. Depending on the shape of the particles of interest, different resonances may evolve. For a spheroid, two resonance condition form—due to the existence of a minor- and major-axis.
For larger particles where the size approaches the wavelength of the exciting field, Maxwell's equations have to be solved. For spheres, Mie-scattering theory can be used. For structures of arbitrary form, the solution can only be found by solving Maxwell's equations—one approach is to use surface or volume integral methods based on Green's function [6].

Integral Method Based on Green's Function

4

A concept typically used in scattering problems is that of the electric field generated by a radiating electric dipole, which also will be the approach in this case. The relationship between a radiating point source, $\vec{j}$ and the resulting electrical field, $\vec{E}$ at some arbitrary point, $\vec{r}$ is partly described through a tensor, $\overleftrightarrow{G}$ which is termed the Green's function (cf. Figure 4.1). The road towards a description of the

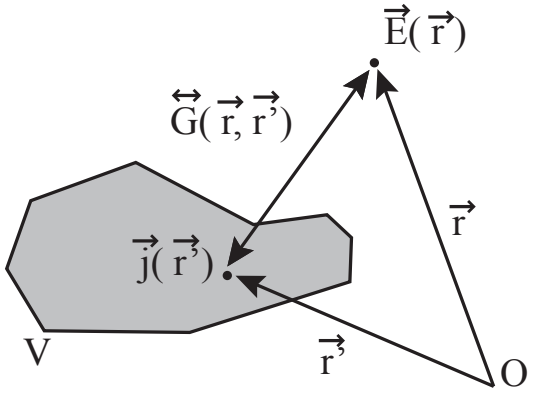

Figure 4.1: Illustration of the Green's tensor and how it relates to a generated electric field due to a point source, $\vec{j}$.

Green's function and its use will take its start by finding the wave equations based on Maxwell's equations. If Maxwell's curl equations are expressed by use of the constitutive relations in Equation (2.2) they yield:

$$\begin{aligned} \nabla \times \vec{E} &= i\omega\mu_0 \overleftrightarrow{\mu} \vec{H}, \\ \nabla \times \vec{H} &= -i\omega\varepsilon_0 \overleftrightarrow{\varepsilon} \vec{E} + \overleftrightarrow{\sigma} \vec{E} + \vec{j}_s. \end{aligned}$$

Next step is to express e.g. the first equation in terms of the second. This is done by taking the curl of the first equation and inserting the second into it. When the curl is taken on the right hand side of the first equation in order to make the insertion of the second equation a problem arises. Generally, the permeability is a function of position and it can not trivially be interchanged with the curl operator. To circumvent this, a restriction to the use of the equation has to be made. In homogeneous media the material parameters are independent of position and so the permeability can safely be taken outside the curl operator, then of course it has to be kept in mind

that from this point the equation only apply for homogeneous media. The first wave equation yields:

$$\begin{aligned}\nabla\times\nabla\times\vec{E} &= i\omega\mu_0\overleftrightarrow{\mu}(\nabla\times\vec{H})\Rightarrow\\ \nabla\times\nabla\times\vec{E} &= \frac{\omega^2}{c^2}\overleftrightarrow{\mu}\left(\overleftrightarrow{\varepsilon}+\frac{i\overleftrightarrow{\sigma}}{\omega\varepsilon_0}\right)\vec{E}+i\omega\mu_0\overleftrightarrow{\mu}\vec{j}_s,\end{aligned} \tag{4.1}$$

where it has been used that $\frac{1}{c}=\sqrt{\varepsilon_0\mu_0}$. Similarly, the wave equation for the magnetic field yields:

$$\nabla\times\nabla\times\vec{H} = \frac{\omega^2}{c^2}\overleftrightarrow{\mu}\left(\overleftrightarrow{\varepsilon}+\frac{i\overleftrightarrow{\sigma}}{\omega\varepsilon_0}\right)\vec{H}+\nabla\times\vec{j}_s. \tag{4.2}$$

The expressions in parenthesis are actually complex dielectric constants and commonly the meaning of $\overleftrightarrow{\varepsilon}$ is redefined so that $\left(\overleftrightarrow{\varepsilon}+\frac{i\overleftrightarrow{\sigma}}{\omega\varepsilon_0}\right)\equiv\overleftrightarrow{\varepsilon}$. A further step can be taken after this. If the identity $\nabla\times\nabla\times\vec{A}=\nabla(\nabla\cdot\vec{A})-\nabla^2\vec{A}$ is used and Maxwell's divergence equations are applied one arrives at what is known as the inhomogeneous Helmholtz equations:

$$\begin{aligned}\left(\nabla^2+k_0^2\overleftrightarrow{\mu}\overleftrightarrow{\varepsilon}\right)\vec{E} &= -i\omega\mu_0\overleftrightarrow{\mu}\vec{j}_s+\frac{1}{\varepsilon_0}\overleftrightarrow{\varepsilon}^{-1}\nabla\rho,\\ \left(\nabla^2+k_0^2\overleftrightarrow{\mu}\overleftrightarrow{\varepsilon}\right)\vec{H} &= -\nabla\times\vec{j}_s,\end{aligned} \tag{4.3}$$

where $k_0=\frac{\omega}{c}$ is the wave number in vacuum. If no source current or charges are present, the equations reduce to the homogeneous Helmholtz equations.
At this point it may be suitable to go through some general properties concerning linear differential equations. If a linear operator acts on a vector field and the result equals a known source function (exactly as in the above problem) one has to find an arbitrary particular solution and add it to the homogeneous solution in order to obtain the full solution. It is assumed that the homogeneous solution, $\vec{A}_0$ for $\vec{B}=0$ is known. The differential equation to be solved is:

$$\mathcal{L}\vec{A}(\vec{r}) = \vec{B}(\vec{r}). \tag{4.4}$$

In the process of finding a solution to this equation one may encounter some difficulties, but a clever trick is to consider the function $\delta(\vec{r}-\vec{r'})$. One can thus write:

$$\mathcal{L}\overleftrightarrow{G}(\vec{r},\vec{r'}) = \overleftrightarrow{I}\delta(\vec{r},\vec{r'}), \tag{4.5}$$

where $\overleftrightarrow{I}$ is the unit tensor. If $\vec{B}(\vec{r'})$ is multiplied onto the equation and each side is integrated, one arrives at:

$$\int_V \mathcal{L}\overleftrightarrow{G}(\vec{r},\vec{r'})\vec{B}(\vec{r'})\mathrm{d}V' = \vec{B}(\vec{r}). \tag{4.6}$$

By comparison, the solution to Equation (4.4) yields:

$$\vec{A}(\vec{r}) = \int_V \overleftrightarrow{G}(\vec{r},\vec{r'})\vec{B}(\vec{r'})\mathrm{d}V'. \tag{4.7}$$

The solution, $\vec{A}$ is in other words found by integrating the Green's function, $\overleftrightarrow{G}$ multiplied with the inhomogeneity, $\vec{B}$ over the source volume, V.
Continuing with the wave equation for the electrical field:

$$\nabla \times \nabla \times \vec{E} - k_0^2 \overleftrightarrow{\mu} \overleftrightarrow{\varepsilon} \vec{E} = i\omega\mu_0 \overleftrightarrow{\mu} \vec{j}_s, \tag{4.8}$$

one can define a Green's function for each component of $\vec{j}_s$. For the x-component of $\vec{j}_s$ it is:

$$\nabla \times \nabla \times \vec{G}_x(\vec{r},\vec{r'}) - k_0^2 \overleftrightarrow{\mu}(\vec{r}) \overleftrightarrow{\varepsilon}(\vec{r}) \vec{G}_x(\vec{r},\vec{r'}) = \delta(\vec{r},\vec{r'})\hat{x}, \tag{4.9}$$

where $\hat{x}$ is a unit vector in the x-direction. Similar equations apply for a point source in the other directions. In order to account for an arbitrary orientation of a point source, the Green's function must take on the form of a tensor and the Green's function for the electrical field is thus defined as:

$$\nabla \times \nabla \times \overleftrightarrow{G}(\vec{r},\vec{r'}) - k_0^2 \overleftrightarrow{\mu}(\vec{r}) \overleftrightarrow{\varepsilon}(\vec{r}) \overleftrightarrow{G}(\vec{r},\vec{r'}) = \overleftrightarrow{I}\delta(\vec{r},\vec{r'}). \tag{4.10}$$

The columns of the Green's function thus corresponds to a field due to a point source directed in either the x-, y-, or z-direction. The source current, $\vec{j}_s$ can be thought of as a superposition of point currents and if an integration over the volume containing the currents is performed, a particular solution to the wave equation can be expressed as (cf. Equation (4.7)):

$$\vec{E}(\vec{r}) = i\omega\mu_0 \overleftrightarrow{\mu}(\vec{r}) \int_V \overleftrightarrow{G}(\vec{r},\vec{r'}) \vec{j}_s(\vec{r'}) \mathrm{d}V'. \tag{4.11}$$

To arrive at a general solution to the wave equation, the homogeneous solution $\vec{E}_0$ must be added to the particular solution and the full solution for the electrical field is:

$$\vec{E}(\vec{r}) = \vec{E}_0(\vec{r}) + i\omega\mu_0 \overleftrightarrow{\mu} \int_V \overleftrightarrow{G}(\vec{r},\vec{r'}) \vec{j}_s(\vec{r'}) \mathrm{d}V'. \tag{4.12}$$

Similar, the solution for the magnetic field turn out to be:

$$\vec{H}(\vec{r}) = \vec{H}_0(\vec{r}) + \int_V \left(\nabla \times \overleftrightarrow{G}(\vec{r},\vec{r'}) \right) \vec{j}_s(\vec{r'}) \mathrm{d}V'. \tag{4.13}$$

These equations are only valid outside the volume V, as a singularity of $\overleftrightarrow{G}$ is experienced for $\vec{r} = \vec{r'}$ [11].
The formalism for the use of Green's function has been established and what is needed next in order to model a scattering problem is the actual form of Green's function, $\overleftrightarrow{G}$. This can be achieved by considering the vector potential $\vec{A}$ and the scalar potential ϕ—these are defined by [11]:

$$\begin{aligned} \vec{E} &= i\omega\vec{A} - \nabla\phi, \\ \vec{H} &= \frac{1}{\mu_0\mu} \nabla \times \vec{A}. \end{aligned} \tag{4.14}$$

Through use of the constitutive relations, the relations in Equation (4.14) are inserted into Maxwell's curl equation for the magnetic field:

$$\nabla \times \frac{1}{\mu_0 \mu} \nabla \times \vec{A} = -i\omega\varepsilon_0\varepsilon \left(i\omega\vec{A} - \nabla\phi \right) + \vec{j}_s. \tag{4.15}$$

The potentials are not fully defined through the relations in Equation (4.14) and using a so-called gauge condition will solidify their relationship. One specific condition—the Lorenz gauge—is defined as:

$$\nabla \cdot \vec{A} = i\omega\mu_0\mu\varepsilon_0\varepsilon\phi. \tag{4.16}$$

Using the Lorenz gauge as well as the identity $\nabla \times \nabla \times \vec{A} = \nabla(\nabla \cdot \vec{A}) - \nabla^2\vec{A}$ one arrive at:

$$\left(\nabla^2 + k_0^2\mu\varepsilon\right)\vec{A} = -\mu_0\mu\vec{j}_s. \tag{4.17}$$

In practice, the above identity can be written as three separate scalar equations, and the scalar Green's function, G_0 can be defined if the source term is replaced by a point source as:

$$\left(\nabla^2 + k_0^2\mu\varepsilon\right) G_0(\vec{r}, \vec{r'}) = -\delta(\vec{r}, \vec{r'}). \tag{4.18}$$

The vector potential in Equation (4.17) can by use of Equation (4.7) be expressed in terms of G_0 as:

$$\vec{A}(\vec{r}) = \mu_0\mu(\vec{r}) \int_V G_0(\vec{r}, \vec{r'}) \vec{j}_s(\vec{r'}) \mathrm{d}V'. \tag{4.19}$$

G_0 is found through its definition in Equation (4.18). According to [11], the only physical solutions are:

$$G_0(\vec{r}, \vec{r'}) = \frac{\mathrm{e}^{\pm ik_0\sqrt{\mu\varepsilon}|\vec{r} - \vec{r'}|}}{4\pi|\vec{r} - \vec{r'}|}. \tag{4.20}$$

The solution with a minus in the exponential describes a spherical wave that goes towards the origin, whereas the other solution denotes a wave propagating away from the origin. Of course it is only the solution with the plus sign which is applicable in the current context.
The scalar Green's function has been found and in the following, it will be expanded to its tensor form. If the Lorenz gauge, Equation (4.16) is inserted into the equation for the electrical field found in Equation (4.14) one gets:

$$\begin{aligned} \vec{E} &= i\omega\vec{A} - \frac{1}{i\omega\mu_0\mu\varepsilon_0\varepsilon} \nabla(\nabla \cdot \vec{A}) \Rightarrow \\ \vec{E} &= i\omega \left(1 + \frac{1}{k_0^2\mu\varepsilon} \nabla\nabla\cdot \right) \vec{A}. \end{aligned} \tag{4.21}$$

The way, the elements of the Green's tensor were defined in Equation (4.9), the source current is $\vec{j}_s(\vec{r'}) = \frac{1}{i\omega\mu_0\mu}\delta(\vec{r},\vec{r'})\hat{x'}$. Inserting this into the equation for the vector potential (Equation (4.19)) yields:

$$\begin{aligned} \vec{A}(\vec{r}) &= \frac{1}{i\omega}\int_V G_0(\vec{r},\vec{r'})\delta(\vec{r},\vec{r'})\hat{x'}\mathrm{d}V' \Rightarrow \\ \vec{A}(\vec{r}) &= \frac{1}{i\omega}G_0(\vec{r},\vec{r'})\hat{x}. \end{aligned} \tag{4.22}$$

Inserting this into Equation (4.21) and remembering the relation between $\vec{E}$ and $\vec{G}_x$ gives:

$$\vec{G}_x(\vec{r},\vec{r'}) = \left(1 + \frac{1}{k_0^2\mu\varepsilon}\nabla\nabla\cdot\right) G_0(\vec{r},\vec{r'})\hat{x}. \tag{4.23}$$

Combining the columns of $\overleftrightarrow{G}$ ends the road taken towards introducing the formalism and finding the form of the Green's function—in its final form the Green's function yields:

$$\overleftrightarrow{G}(\vec{r},\vec{r'}) = \left(\overleftrightarrow{I} + \frac{1}{k_0^2\mu\varepsilon}\nabla\nabla\right) G_0(\vec{r},\vec{r'}), \tag{4.24}$$

where the definition $\nabla\cdot(G_0\overleftrightarrow{I}) = \nabla G_0$ has been used.
This form of the Green's function only applies for a tree dimensional space. Furthermore the restriction made earlier about a homogeneous media has to be respected. For e.g. a two dimensional problem, one thus have to find another expression for the Green's function—although the formalism itself is still valid.

Near-Field Modelling

5

When dealing with the modelling of the electrical field around a one-dimensional grating, it is convenient to only make calculations in two dimensions, since this results in simpler programs and thus faster processing. A grating as illustrated in Figure 5.1 is used in connection with the integral method outlined in Chapter 4 and modelled in the following. A plane wave with wave vector $\vec{k}(x,y)$ is incident on

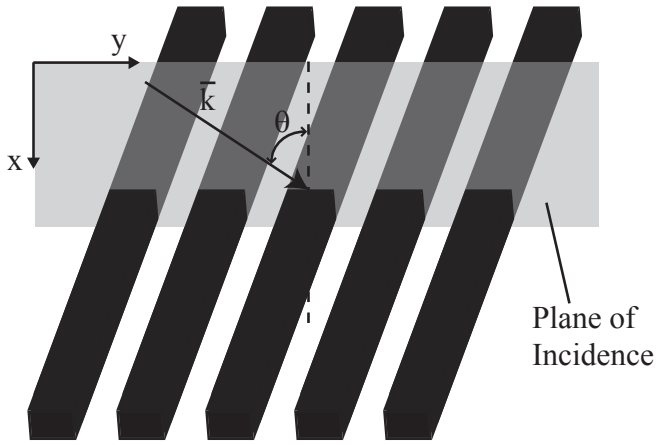

Figure 5.1: One-dimensional grating with x- and y-axis as shown and z-axis along the grating-wires.

the structure and the electrical field is assumed to be oriented along the z-axis. The incident wave can thus be described as:

$$E_0(x,y) \quad = \quad \mathrm{e}^{-ik_0\sqrt{\varepsilon_{ref}}(x\cos(\theta)+y\sin(\theta))}, \tag{5.1}$$

where it is assumed that the reference medium is non-magnetic and thus $\mu_{ref} = 1$. The incoming field is thus a solution to the homogeneous Helmholtz equation $\left(\nabla^2 + k_0^2\varepsilon_{ref}\right)E_0(x,y) = 0$. In order to determine the field distribution in the problem at hand, the electrical field which emerges due to scattering in the grating structure has to be found—i.e. a solution to the inhomogeneous Helmholtz equation is needed. From Maxwell's curl equation for the magnetic field, where it is assumed that no source current and only the induced electric current, $\vec{j}_e$ exist, one gets:

$$\nabla \times \vec{H} \quad = \quad -i\omega\varepsilon_0\varepsilon_{ref}\vec{E} + \vec{j}_e. \tag{5.2}$$

When an object such as the grating is present in the reference system, the dielectric response of the object relative to the reference is equal to $(\varepsilon - \varepsilon_{ref})$, where ε is the

dielectric constant of the perturbing object [11]. The induced electric current thus takes the form:

$$\vec{j_e} = -i\omega\varepsilon_0(\varepsilon - \varepsilon_{ref})\vec{E}. \tag{5.3}$$

Using this, along with the formalism reviewed in Chapter 4, the full solution can be written as:

$$E(x,y) = E_0(x,y) + i\omega\mu_0 \int_A g(x,y;x',y') j_e(x',y') \mathrm{d}x'\mathrm{d}y', \tag{5.4}$$

where it has been assumed that also the grating media is non-magnetic. Introducing j_e explicitly yields:

$$E(x,y) = E_0(x,y) + k_0^2 \int g(x,y;x',y')(\varepsilon(x',y') - \varepsilon_{ref})E(x',y')\mathrm{d}x'\mathrm{d}y'. \tag{5.5}$$

It was mentioned in Chapter 4 that the found Green's function only applied for three-dimensional problems. The Green's function used in Equation (5.5) is given by [16]:

$$g(x,y;x',y') = \frac{1}{4i} H_0^{(2)} \left(k_0 \sqrt{(x-x')^2 + (y-y')^2} \right), \tag{5.6}$$

where $H_0^{(2)}(k_0 r)$ is the zeroth order Hankel function of the second kind with respect to the argument $k_0 r$. For reference, the functions are depicted in Figure 5.2. Equation (5.5) can be solved numerically if the grating structure is resolved into a

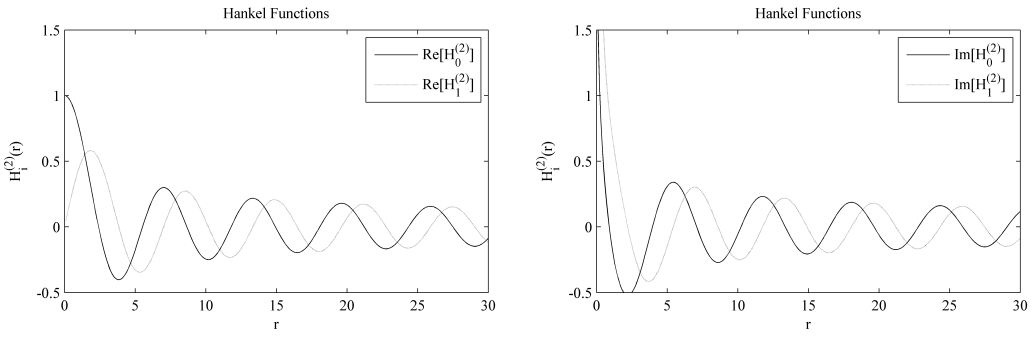

(a) (b)

Figure 5.2: The zeroth and first order Hankel functions of the second kind. (a) Real part of the Hankel functions. (b) Imaginary part of the Hankel functions.

number of area elements centred at all (x_i, y_i) points—the integral thus takes on the form of a sum over N elements with area ΔA. The value of the electrical field at (x_i, y_i) is approximated to apply for the entire area ΔA_i related to that point. In this way, a set of equations are obtained—all on the form:

$$E_i = E_{0,i} + k_0^2 \sum_j g_{ij}(\varepsilon_j - \varepsilon_{ref}) E_j \Delta A_j, \tag{5.7}$$

with $g_{ij} = g(x_i, y_i; x_j, y_j)$. Since these equations are all coupled, it is necessary to first solve the system for the grating structure itself and then subsequently use the obtained result for finding the field outside the grating structure. As mentioned in Chapter 4, there exists a problem with the Green's function being singular inside the source volume/area—namely at points $i = j$, which is why the equation is only valid outside the source. Fortunately, one can make an approximation—using a circular area element with the same size as the rectangular or square area element chosen: $\Delta A = \pi a^2$, where a is the radius of the circle. The approximation yield [16]:

$$g_{ii} \approx \frac{1}{2i(k_0 a)^2}\left(k_0 a H_1^{(2)}(k_0 a) - i\frac{2}{\pi}\right), \tag{5.8}$$

where $H_1^{(2)}$ is the first order Hankel function of the second kind (cf. Figure 5.2). Using this, it is now possible to evaluate the electric field inside the source structure.

Due to the periodicity in the y-direction, it should be sufficiently to look at the resulting field across a single wire. However, the scattered field from each wire may influence other wires, which then in return again may have an increased influence on the field from the 'first' wire. In order to obtain a valid result, it is therefore necessary to include several wires in the calculation—even though the field is only rendered across a single grating period. For a start, one should determine the number of barriers to include in the calculations. In Figure 5.3, different numbers of wires are included in the model. The barriers are 60 nm$\times$300 nm in size and placed with a 600 nm periodicity. The incoming field, E_0 arrives normal to the grating, i.e. $\theta = 0$ and the wavelength of it is 633 nm. The barriers are given the material parameters of gold, while the reference material is vacuum and thus $\varepsilon_{ref} = 1$. As expected, it is seen that the field is enhanced with an increasing number of barriers. It is also seen that the field enhancement is primarily located in the space between the barriers. Now to the question of how many barriers to include; it is quite clear that one is not enough. If the field between the bottom barrier and the second barrier from the bottom in Figure 5.3(c) is observed and compared to the field between the two bottom barriers of Figure (d), it is seen that a slightly increase in intensity is present. This increase is due to the contribution from primarily the second top-most barrier. It cannot be ruled out that also the top barrier has an effect, but this contribution is thought to be vanishing. It is thus decided to look at the field emanating from a total of six barriers—with focus on the field enhancement between the two middle barriers. The number of six barriers is also partly chosen with computing hardware in mind—with the used resolution, a seventh and eighth barrier could not be included due to memory requirements of the program. Due to the memory requirement, also the silicon background has been omitted, why come the observed field enhancements may differ from e.g. experimental results obtained by near-field microscopy.
The dependence of wavelength on field enhancement is investigated in the following. Calculating and rendering the fields due to all different incoming fields with wavelength in e.g. the visible regime quickly become overwhelming. Therefore is an area of only six nm's width at the edge of the barriers rendered for a range of

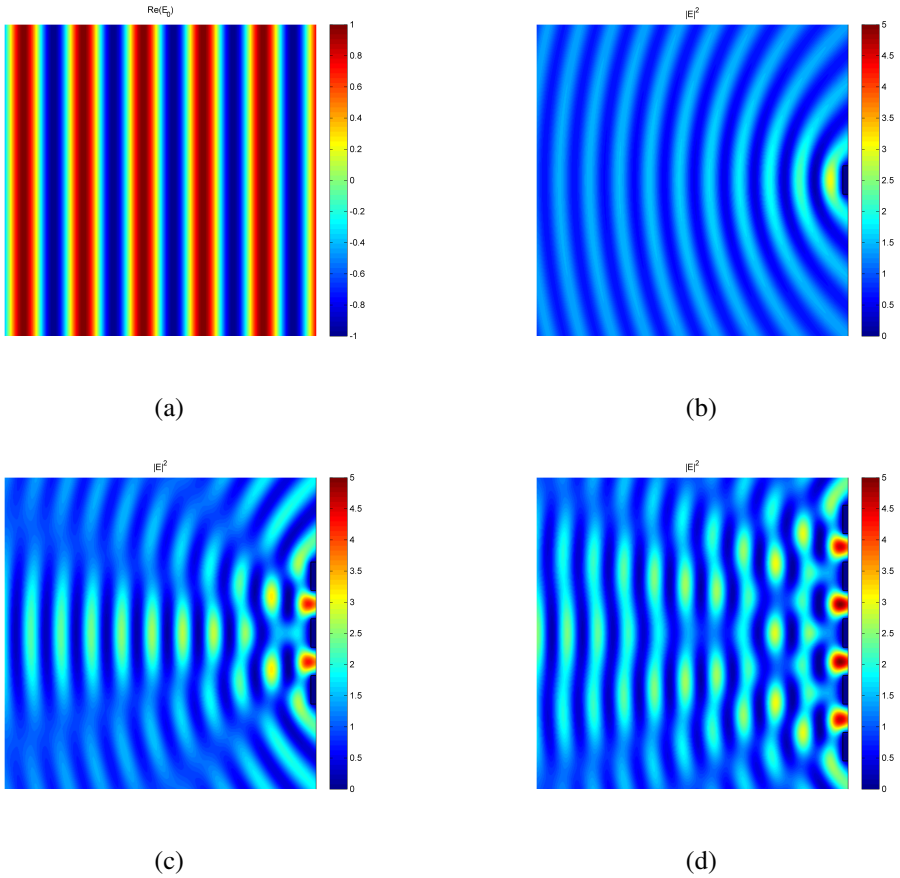

Figure 5.3: Model of the electrical field from a number of gold barriers subjected to a monochromatic field with a wavelength of 633 nm. (a) Real part of the exciting electrical field. (b) The absolute square of the field due to one gold barrier. (c) The absolute square of the field due to three gold barriers. (d) The absolute square of the field due to five gold barriers.

wavelengths and this result is taken as an expression for the overall field enhancement. Figure 5.4 illustrates this result. Three wavelengths seem interesting at first glance, namely ≈480 nm, ≈510 nm, and ≈640 nm—these wavelengths are marked with dashed lines. The largest field enhancements are observed around λ =480nm and λ =640nm. However, it is not given that the field is enhanced the most at these wavelengths—the observed change in intensity may also emanate from a spatial shift of the enhancement, i.e. the enhancement may move further along in between the barriers or farther apart from them.

In Figure 5.5 is the resulting field from a wavelength of 640 nm rendered—flanked by results for λ =610 nm and λ =670 nm. It is seen that the field is enhanced further from λ =610 nm to λ =640 nm. Despite from what could have been expected from Figure 5.4, the field is further enhanced towards λ =670 nm. It is seen that the centre of the enhancement is still located between the barriers, but that it moves away from them, i.e. the field is to a better degree localised above the grating surface than in between the grating wires.

Figure 5.6 shows an image of the absolute square of the field due to a wavelength

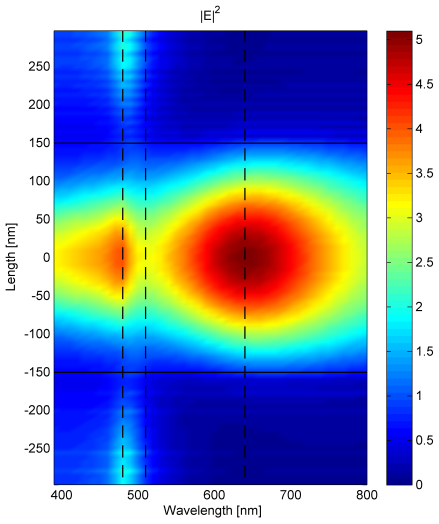

Figure 5.4: Field enhancement between barriers as a function of wavelength—the horizontal lines mark the sides of the barriers. The contribution from six barriers has been included in the calculation.

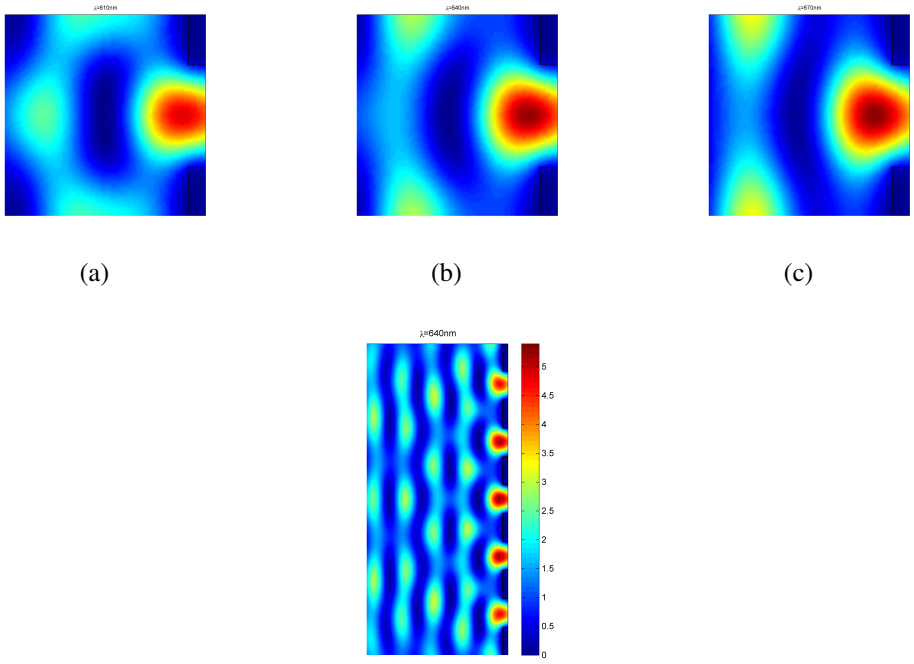

(a) (b) (c)

(d)

Figure 5.5: The absolute square of a field around two gold barriers. (a) Wavelength, λ =610 nm. (b) Wavelength, λ =640 nm. (c) Wavelength, λ =670 nm. (d) Same as Figure (b), but a larger area has been rendered in order to have a better overview.

of 480 nm plotted—flanked by results for λ =450 nm and λ =510 nm. It is seen that very large field enhancements are observed at λ =480 nm—at least compared to the enhancements noted at other wavelengths. There are still observed enhance-

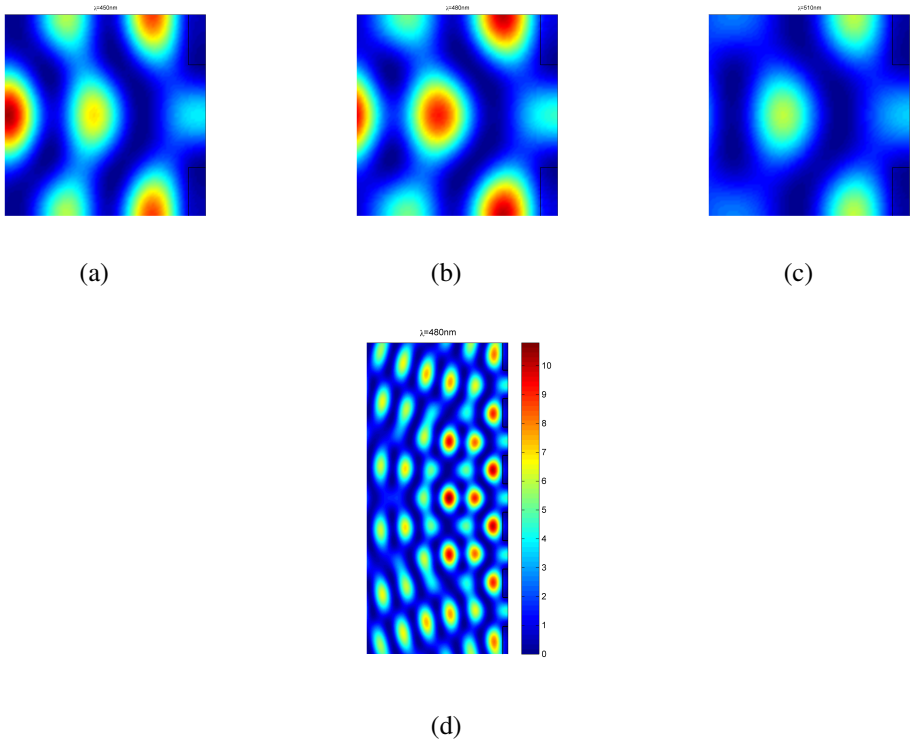

Figure 5.6: The absolute square of a field around two gold barriers. (a) Wavelength, λ =450 nm. (b) Wavelength, λ =480 nm. (c) Wavelength, λ =510 nm. (d) Same as Figure (b), but a larger area has been rendered in order to have a better overview.

ments between the barriers, but smaller than around e.g. λ =640 nm instead there are localised maxima farther away from the barriers, i.e. the surface of the grating. Furthermore, localised maxima are found on top of the gold wires, which around λ =480 nm extend into the barrier itself—this is most clearly seen in Figure 5.4. The maxima still exist as the wavelength is altered towards λ =510 nm, but the intensity drops a great deal.
The results can possibly be explained by looking at the refractive index for gold (cf. Figure 5.7). It is seen that the maximum noted in Figure 5.4 around λ =480 nm lies around the interband transition of gold.
According to Schider *et al.* [15], experimental results show that the extinction maximum in the spectra from a silver grating red-shifts with increasing wire width. If this also applies for gold nano wires, one can possibly tailor the desired resonance frequency for the sensing application. However, in production this also require even more precise manufacturing as a deviation from the wanted grating specification may result in a false positive or negative, when the sensor is used. To see if the width is of importance in general, it is varied at a specific wavelength. The result is seen in Figure 5.8. Again a 6 nm wide area from the outermost edge of the barriers is used to represent the entire result from each barrier width. It is seen that the width of the barriers indeed have an impact on the field enhancement between the barriers. In order to clarify if the observed phenomenon in Figure 5.8 is due to altered field strength or placement of the enhancement, a larger area is rendered at the specified

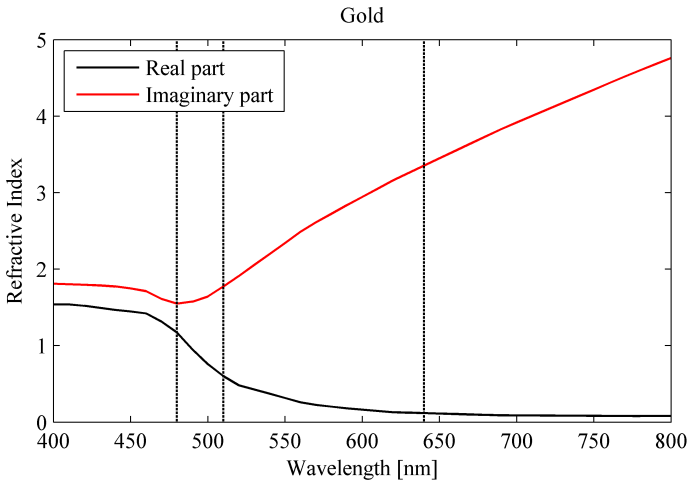

Figure 5.7: Refractive index of gold.

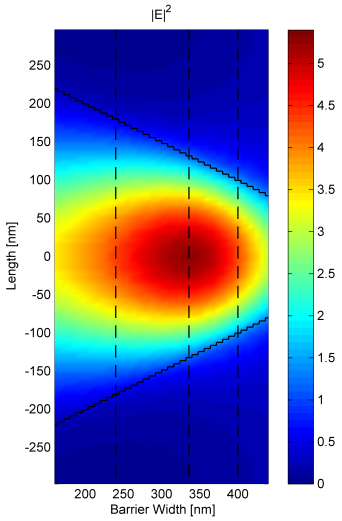

Figure 5.8: Field enhancement between barriers as a function of barrier width. The contribution from six barriers has been included in the calculation and the wavelength used was λ =640 nm.

barrier widths—namely 240 nm, 336 nm, and 400 nm. These are shown in Figure 5.9. The field enhancement is seen to increase with the width of the barriers. At the same time the enhancement is displaced farther away from the barriers—also with increasing width. Actually—qualitatively, the same pattern in the development of the field enhancement can be seen for both the increase in barrier width and the increase in wavelength around 640 nm—also cf. Figures 5.5 and 5.9.
As mentioned, the above results stem from an *s*-polarised exciting field. When looking at experimental data, the observed general field enhancements should be kept in mind—such that observed responses are not wrongfully ascribed to excitation of plasmon resonances.

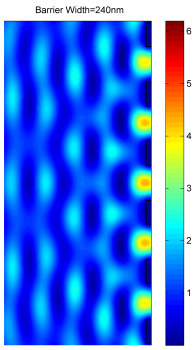

(a)

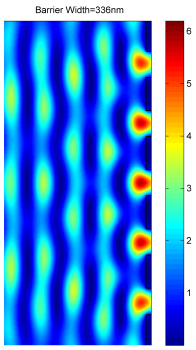

(b)

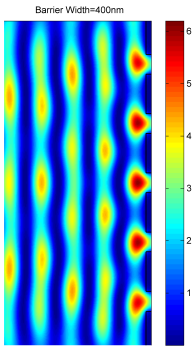

(c)

Figure 5.9: The exciting field is with wavelength, λ =640 nm. (a) Barrier width is 240 nm. (b) Barrier width is 336 nm. (c) Barrier width is 400 nm.

Second Harmonic Generation

6

It was chosen to investigate the second harmonic response of the produced gratings. For this purpose, the theoretical concept is reviewed in the following.
Once again the starting point is Maxwell's equations (cf. Equation (2.4)). The curl is taken of Maxwell's curl equation for the electrical field and subsequent the curl equation for the magnetic field is inserted by use of the constitutive relations (cf. Equation (2.2)):

$$\begin{aligned} \nabla\times\nabla\times\vec{E} &= i\omega\mu_0\overleftrightarrow{\mu}\nabla\times\vec{H} \Rightarrow \\ \nabla\times\nabla\times\vec{E} &= \omega^2\mu_0\varepsilon_0\overleftrightarrow{\mu}\vec{E}+\omega^2\mu_0\overleftrightarrow{\mu}\vec{P}+i\omega\mu_0\overleftrightarrow{\mu}\vec{j}. \end{aligned} \tag{6.1}$$

The polarisation can be expressed as a sum of the linear and all non-linear contributions as:

$$\vec{P} = \vec{P}^{(1)}+\vec{P}^{(2)}+\vec{P}^{(3)}+\ldots. \tag{6.2}$$

The dielectric constant can be expanded in a similar way and one can write:

$$\varepsilon_0\vec{E}+\vec{P} = \varepsilon_0\overleftrightarrow{\varepsilon}^{(1)}\vec{E}+\vec{P}^{(2)}+\vec{P}^{(3)}+\ldots. \tag{6.3}$$

In the present context, only non-linear contributions to the second order are of interest and the remaining non-linear contributions are discarded before insertion into Equation (6.1). It is further assumed that no source currents and charges are present and through use of $\nabla\times\nabla\times\vec{A}=\nabla(\nabla\cdot\vec{A})-\nabla^2\vec{A}$, the following inhomogeneous Helmholtz equation is obtained:

$$\left(\nabla^2+k_0^2\overleftrightarrow{\mu}\overleftrightarrow{\varepsilon}^{(1)}\right)\vec{E} = -\omega^2\mu_0\overleftrightarrow{\mu}\vec{P}^{(2)}. \tag{6.4}$$

This equation can thus be understood as the description of an electrical field, $\vec{\mathcal{E}}(2\omega)$ driven by the second order polarisation, $\vec{P}^{(2)}$.
In the following, it is assumed that the second order polarisation is originating from a single electrical field, $\vec{\mathcal{E}}(\omega)$, i.e. sum- and difference-frequency generation simplify to optical rectification and second harmonic generation—also known as frequency doubling. The second order polarisation, $\vec{P}^{(2)}=\varepsilon_0\overleftrightarrow{\chi}_e^{(2)}\vec{\mathcal{E}}(\omega)\vec{\mathcal{E}}(\omega)$ can thus be found through the determination of the second order susceptibility, $\overleftrightarrow{\chi}_e^{(2)}$. What is important in this context is the resonance conditions, an explicit expression for the susceptibility will therefore be omitted and only the resonance conditions will be reviewed. Finding the susceptibility can be done through a quantum mechanical approach based on perturbation theory. The system, i.e. the material subjected to

the electrical field is in its unperturbed state described by eigenstates related to the time-independent Schrödinger equation:

$$\hat{H}_0|\varphi_n\rangle = E_n|\varphi_n\rangle, \tag{6.5}$$

where $\hat{H}_0 = -\frac{\hbar^2}{2m}\nabla^2 + V(\vec{r},t)$ is the Hamiltonian operator related to the unperturbed case and the eigenstates constitute any wave function, $|\psi\rangle$, as:

$$|\psi\rangle = \sum_n a_n|\varphi_n\rangle e^{-iE_nt/\hbar}. \tag{6.6}$$

It is assumed that the eigenstates are known and that the only unknown is the time-dependent coefficient, a_n which can be thought of as the probability amplitude and thus $|a_n|^2$ is the probability of finding the system in the state $|\varphi_n\rangle$ at time t. If the system is perturbed by an external perturbation—in this case an electrical field—the Hamiltonian changes into $\hat{H} = \hat{H}_0 + \frac{1}{2}\hat{H}_1 e^{-i\omega t} + \frac{1}{2}\hat{H}_1^\dagger e^{i\omega t}$, where $\hat{H}_1$ denotes the spatial part of the perturbation. It is assumed that the time-dependence of the perturbation is harmonic and in order to describe the time-dependent response of the system, the time-dependent Schrödinger equation must be solved:

$$i\hbar\frac{\partial|\psi\rangle}{\partial t} = \left(\hat{H}_0 + \frac{1}{2}\hat{H}_1 e^{-i\omega t} + \frac{1}{2}\hat{H}_1^\dagger e^{i\omega t}\right)|\psi\rangle. \tag{6.7}$$

Inserting the wave function from Equation (6.6) and carrying out the differentiation yields:

$$\sum_n \left(a_n E_n|\varphi_n\rangle + i\hbar\frac{\partial a_n}{\partial t}|\varphi_n\rangle\right) e^{-iE_nt/\hbar} =$$
$$\sum_n a_n \left(\hat{H}_0|\varphi_n\rangle + \frac{1}{2}\hat{H}_1|\varphi_n\rangle e^{-i\omega t} + \frac{1}{2}\hat{H}_1^\dagger|\varphi_n\rangle e^{i\omega t}\right) e^{-iE_nt/\hbar}. \tag{6.8}$$

Utilising the eigenvalue condition, the first terms on the left- and right-hand sides cancel and the equation reduces to:

$$\sum_n \frac{\partial a_n}{\partial t}|\varphi_n\rangle e^{-iE_nt/\hbar} = \frac{1}{2i\hbar}\sum_n a_n \left(\hat{H}_1|\varphi_n\rangle e^{-i\omega t} + \hat{H}_1^\dagger|\varphi_n\rangle e^{i\omega t}\right) e^{-iE_nt/\hbar}. \tag{6.9}$$

The eigenstates are mutually orthonormal and thus they satisfy the relation $\langle\varphi_m|\varphi_n\rangle = \delta_{nm}$, where the notation implies:

$$\langle\varphi_m|\varphi_n\rangle = \int \varphi_m^*\varphi_n d^3r. \tag{6.10}$$

Next step is to multiply Equation (6.9) with $\langle\varphi_m|$ from the left and integrate to yield:

$$\frac{\partial a_m}{\partial t} = \frac{1}{2i\hbar}\sum_n a_n \left(H_{mn}e^{-i\omega t} + H_{mn}^\dagger e^{i\omega t}\right) e^{iE_{mn}t/\hbar}, \tag{6.11}$$

where $E_{mn} = E_m - E_n$ and $H_{mn} = \langle\varphi_m|\hat{H}_1|\varphi_n\rangle$. For electromagnetic perturbations, the perturbing Hamiltonian, $\hat{H}_1$ is proportional to the field strength. The coefficient a_m is now expressed in a power series also in terms of field strength:

$$a_m = a_m^{(0)} + a_m^{(1)} + a_m^{(2)} + \ldots. \tag{6.12}$$

In order for Equation (6.11) to be valid, the power in field strength must be the same on each side and since the perturbation is proportional to the field strength, it implies:

$$\frac{\partial a_m^{(p)}}{\partial t} = \frac{1}{2i\hbar}\sum_n a_n^{(p-1)}\left(H_{mn}\mathrm{e}^{-i\omega t} + H_{mn}^{\dagger}\mathrm{e}^{i\omega t}\right)\mathrm{e}^{iE_{mn}t/\hbar}, \tag{6.13}$$

and thus $\frac{\partial a_m^{(0)}}{\partial t} = 0$, from which it follows that no perturbation is present at all—i.e. the system is stationary since the coefficients are constant. The first order coefficient is found by setting $p = 1$ and integrating:

$$\begin{aligned} a_m^{(1)} &= \int_{-\infty}^{t} \frac{\partial a_m^{(1)}}{\partial t'}\mathrm{d}t' \\ &= -\frac{1}{2}\sum_n a_n^{(0)}\left(\frac{H_{mn}\mathrm{e}^{-i\omega t}}{E_{mn}-\hbar\omega} + \frac{H_{mn}^{\dagger}\mathrm{e}^{i\omega t}}{E_{mn}+\hbar\omega}\right)\mathrm{e}^{iE_{mn}t/\hbar}, \end{aligned} \tag{6.14}$$

and in a similar manner can higher order coefficients be found. A desired observable can now be found by determining the expectation value of its corresponding operator, i.e.:

$$\begin{aligned} \langle X\rangle &= \langle\psi|\hat{X}|\psi\rangle = \sum_{m,n} a_m^* a_n \langle\varphi_m|\hat{X}|\varphi_n\rangle \mathrm{e}^{iE_{mn}t/\hbar} \\ &= \sum_{m,n}\left(a_m^{(0)*}a_n^{(0)} + a_m^{(0)*}a_n^{(1)} + a_m^{(1)*}a_n^{(0)} + \ldots\right)\langle\varphi_m|\hat{X}|\varphi_n\rangle\mathrm{e}^{iE_{mn}t/\hbar} \\ &= \langle X^{(0)}\rangle + \langle X^{(1)}\rangle + \ldots, \end{aligned} \tag{6.15}$$

where the $\langle X^{(n)}\rangle$ terms are comprised of coefficient terms with a total order of n. It was previously mentioned that $|a_n|^2$ was in fact the probability of finding the system in the state, φ_n—which thus also must apply for $|a_n^{(0)}|^2$ in the event of an unperturbed system. In thermal equilibrium then, the absolute square of the n'th coefficient is equal to the probability distribution at E_n, which in the present case is the Fermi-Dirac distribution, $f(E_n)$. It can be shown that $a_n^{(0)*}a_m^{(0)} = \delta_{mn}f(E_n)$ [2] from which it follows that the constant term is:

$$\langle X^{(0)}\rangle = \sum_n f(E_n)\langle\varphi_n|\hat{X}|\varphi_n\rangle. \tag{6.16}$$

The linear response—i.e. the first order component of the expansion is:

$$\begin{aligned} \langle X^{(1)}\rangle &= \sum_{m,n}\left(a_m^{(0)*}a_n^{(1)} + a_m^{(1)*}a_n^{(0)} + \ldots\right)\langle\varphi_m|\hat{X}|\varphi_n\rangle\mathrm{e}^{iE_{mn}t/\hbar} \\ &= -\frac{1}{2}\sum_{m,n} f(E_n)\langle\varphi_n|\hat{X}|\varphi_m\rangle\left(\frac{H_{mn}\mathrm{e}^{-i\omega t}}{E_{mn}-\hbar\omega} + \frac{H_{mn}^{\dagger}\mathrm{e}^{i\omega t}}{E_{mn}+\hbar\omega}\right) \\ &\quad -\frac{1}{2}\sum_{m,n} f(E_m)\langle\varphi_n|\hat{X}|\varphi_m\rangle\left(\frac{H_{mn}^{\dagger}\mathrm{e}^{i\omega t}}{E_{nm}-\hbar\omega} + \frac{H_{mn}\mathrm{e}^{-i\omega t}}{E_{nm}+\hbar\omega}\right). \end{aligned} \tag{6.17}$$

The above expression can be decomposed into frequency components:

$$\langle X^{(1)} \rangle = \frac{1}{2} X^{(1)}(\omega) e^{-i\omega t} + \frac{1}{2} X^{(1)*}(\omega) e^{i\omega t}, \tag{6.18}$$

where

$$X^{(1)}(\omega) = -\sum_{m,n} f_{nm} \frac{H_{mn} \langle \varphi_n | \hat{X} | \varphi_m \rangle}{E_{mn} - \hbar\omega}, \tag{6.19}$$

with $f_{nm} = f(E_n) - f(E_m)$. No damping has so far been taken into account, but this can be rectified by subtracting a loss term, $i\hbar\Gamma$ in the denominator of Equation (6.19).
Following the exact same procedure, the second order perturbation can be found. This is done in e.g. [13] and the frequency components are:

$$\langle X^{(2)} \rangle = \frac{1}{2} X^{(2)}(0) + \frac{1}{2} X^{(2)*}(0) + \frac{1}{2} X^{(2)}(2\omega) e^{-i2\omega t} + \frac{1}{2} X^{(2)*}(2\omega) e^{i2\omega t} \tag{6.20}$$

where

$$\begin{aligned} X^{(2)}(0) = -\frac{1}{2} \sum_{m,n,o} \langle \varphi_m | \hat{X} | \varphi_n \rangle \Big(& f(E_m) \frac{H^{\dagger}_{om} H_{no}}{(E_{om} + \hbar\omega) E_{mn}} \\ & + f(E_o) \frac{H^{\dagger}_{om} H_{no}}{(E_{no} - \hbar\omega)(E_{om} + \hbar\omega)} + f(E_n) \frac{H^{\dagger}_{om} H_{no}}{E_{mn} (E_{no} - \hbar\omega)} \Big) \end{aligned} \tag{6.21}$$

and

$$\begin{aligned} X^{(2)}(2\omega) = -\frac{1}{2} \sum_{m,n,o} \langle \varphi_m | \hat{X} | \varphi_n \rangle \Big(& f(E_m) \frac{H_{om} H_{no}}{(E_{om} - \hbar\omega)(E_{mn} + 2\hbar\omega)} \\ & + f(E_o) \frac{H_{om} H_{no}}{(E_{no} - \hbar\omega)(E_{om} - \hbar\omega)} + f(E_n) \frac{H_{om} H_{no}}{(E_{mn} + 2\hbar\omega)(E_{no} - \hbar\omega)} \Big). \end{aligned} \tag{6.22}$$

If the perturbing electrical field with amplitude $\mathcal{E}$ is oriented along $\hat{z}$, the second order response is found by inserting the polarisation density operator, $\hat{P} = -\frac{e\hat{z}}{\Omega}$, where Ω is the unit cell volume—along with the perturbing Hamiltonian $\hat{H}_1 = e\mathcal{E}\hat{z}$. The second order susceptibility is subsequently found by dividing the obtained expression with $\varepsilon_0 \mathcal{E}^2$. It is straightforward to do and does not alter the resonance conditions, which therefore will be discussed with background in Equations (6.21) and (6.22).
The response from Equation (6.21) represent optical rectification which arises from difference frequency generation. The time-independent terms in fact represent a DC electrical field which build up in the material due to the applied oscillating electrical field. Equation (6.22) on the other hand represent the sought second harmonic generated response, which through Equation (6.20) is seen to oscillate with twice

the frequency of the exciting field. The response is seen to maximise when frequency terms in the denominators match the energy difference between two levels. Two different types of excitations can occur. If the pump frequency matches the resonance condition of the material, two photons can be absorbed and the system enters into a virtual energy state from where a second harmonic photon is emitted as the system returns to its ground state. Another possibility is when two photons are absorbed at the same time in such a way that the sum of their frequencies match the resonance condition of the system and the emitted response thus is of that type. The situations are illustrated in Figure 6.1 to the left and right, respectively. When

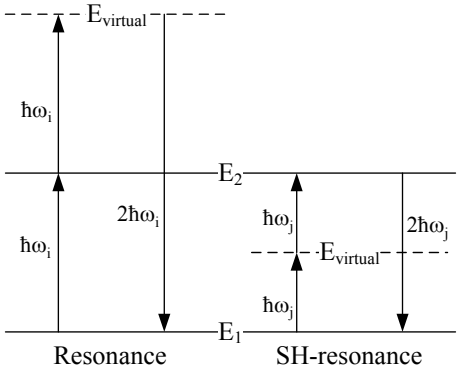

Figure 6.1: Illustration of the resonance conditions in connection with second harmonic generation of an electrical response, where the fundamental frequencies are denoted by ω_i or ω_j and the second harmonic frequencies are denoted by twice the fundamental frequencies.

using the method of second harmonic spectroscopy as a characterisation method, the obtained spectra can thus be interpreted as originating from transitions equal to—or twice—the difference of two energy levels.
In order to obtain a measurable second harmonic response, the electrical field around the sample material has to be relatively strong, which implicit requires the use of a laser. The stronger field—the stronger the second harmonic response which means that e.g. enhanced field strengths in and around metallic particles will result in a stronger response.
Furthermore, certain selection rules apply. No second harmonic response is expected from centrosymmetric materials. Amorphous media are always centrosymmetric whereas crystalline materials may or may not be. A second harmonic response is only expected from materials where the inversion symmetry is broken and thus a bulk response from centrosymmetric materials may occur if the symmetry is obstructed by defects. This contribution is small compared to the response from the surface of the material—where the inversion symmetry is clearly broken. Because of this, second harmonic spectroscopy is extremely surface sensitive. [2]

Experimental

II

In this part, the experimental work will be described. First and foremost, the making of the gratings will be outlined—where procedures and intermediate results will be described—along with considerations concerning the choice of the different parameters used in the process.
Next, the optical setup in connection with measurements will be described and the results from the measurements will be presented and discussed.

Grating-Sample Preparation

7

In this chapter, the production of the samples containing the grating structures will be described. First, an overview of the process is given and subsequent the procedure is described more thorough.

7.1 Overall Procedure

Two types of gratings were produced. One kind, where grooves were etched into a plain silicon wafer which previously had been subjected to a lithographic process. A second kind, where metallic wires (illustrated in Figure 7.1) were deposited onto a plain silicon wafer also after a lithographic process had been done. The silicon

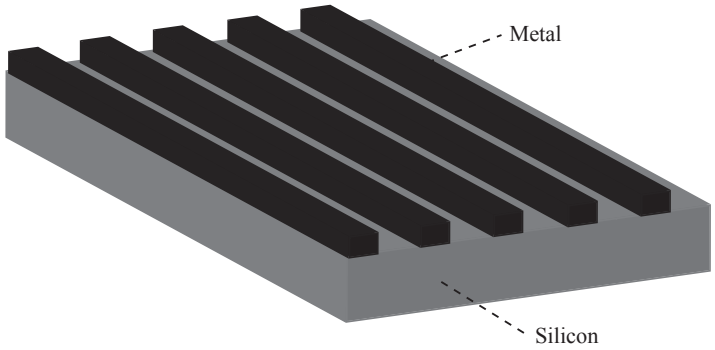

Figure 7.1: Illustration of the desired metallic grating to be created.

wafers were initially cleansed and covered by polymethylmethacrylate (PMMA) which functioned as an e-beam resist. This situation is depicted in Figure 7.2(a), where the top layer is PMMA and the bottom layer is the silicon substrate layer. Next, the mask for the grating was written by e-beam lithography and developed to reveal the actual grating pattern (cf. (b)). The silicon gratings were hereafter etched using reactive ion etching and subsequently finalised be removal of the remaining PMMA. In case of the metallic gratings, the situation in (c) illustrates that a layer of metal has been deposited by means of e-beam evaporation and finally in (d), lift-off has been performed to yield the wanted metal grating. After this, the gratings were characterised by their physical shape and by means of their optical properties.

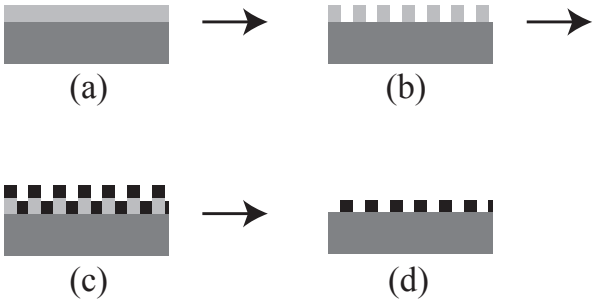

Figure 7.2: Step by step procedure for the making of a one-dimensional grating with a rectangular cross section.

7.2 Deposition of E-beam Resist

The e-beam resist could potentially be of arbitrary thickness with respect to the e-beam writing process, as an appropriate energy dose would have to be found under any circumstance. However, the structure which has to be made in the lithographic process may demand certain criteria for the resist thickness. Due to the nanoscaled features of the grating which had to be produced, requirements for the resist thickness were indeed present and an appropriate thickness of the photo resist had to be chosen.
It was important that the thickness of the resist layer was not too large compared to the period of the grating since this could result in a collapse of the structure as illustrated in Figure 7.3. The reason for such a collapse can be found in the development process. Capillary forces can overcome the elastic restoring forces of the e-beam resist and thus the pattern collapses [3]. The type of resist and the ratio between the resist thickness and the width of the pattern elements are of importance. The upper limit for the resist thickness is set to a value smaller than that of the period of the desired grating. A grating period of 600 nm was chosen for the samples. In Figure 7.9 (f), an example of a pattern collapse is observed. It is, however, believed that the collapse is caused by overexposure and that the strings of resist are partially lifted from the silicon wafer.
The resist thickness could also become to small. Because of the etching or lift-off process which had to be done in a later step, the resist thickness had to be larger than the thickness removed in the etching process or the thickness of the desired metal layer—else, lift-off could be impossible to achieve. This can be understood by inspecting the right-hand side of Figure 7.4 where it is seen that the resist is totally covered by the metal layer—practically hindering the access of the solvent to the PMMA. A grating with approximately 200 nm deep grooves was initially desired

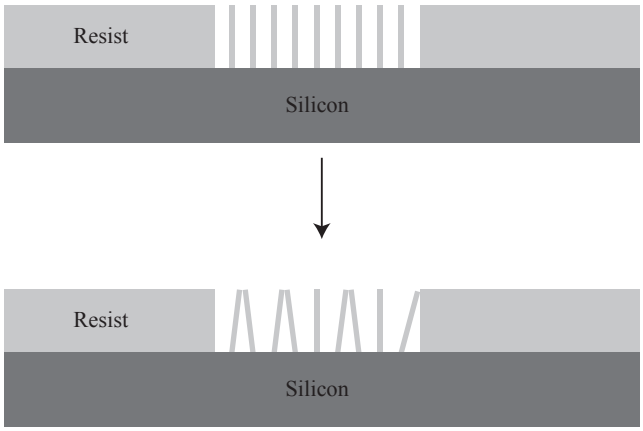

Figure 7.3: Illustration of a situation where a written structure has collapsed.

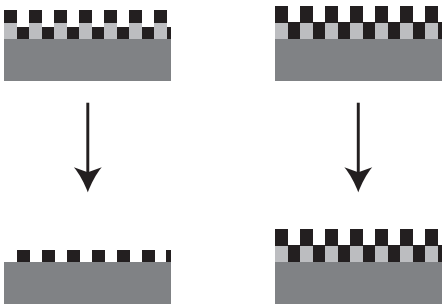

Figure 7.4: Left: Successful lift-off process. Right: Unsuccessful lift-off process.

and thus the lower limit for the resist thickness had been established.
With these requirements in mind, the PMMA layer thickness should be in between approximately 200 nm and 400 nm. A resist layer in the high end of the interval—around 400 nm is preferred, since a thicker resist is less sensitive to small changes in the e-beam current during the lithographic process.
The PMMA was deposited onto the wafers using a spin coater. First, tests were made where different spin settings were used in order to yield different thickness's of the PMMA layer and thus find appropriate settings. Previously—in correlation to another project, similar tests were made. The data from these are presented in Figure 7.5. It is seen that the thickness's which are desired are well covered in the data-set. However, in order to yield a layer thickness around 400 nm, a rather low spin-speed is required. Due to this, non-uniformity of the resist layer is seen and a variation in resist thickness from sample to sample is expected. If the resist thickness varies considerably from sample to sample, it becomes impossible to determine the correct dose of electrons which repeatedly will yield the desired degree of exposure in the lithographic process. Therefore, settings are sought which yield

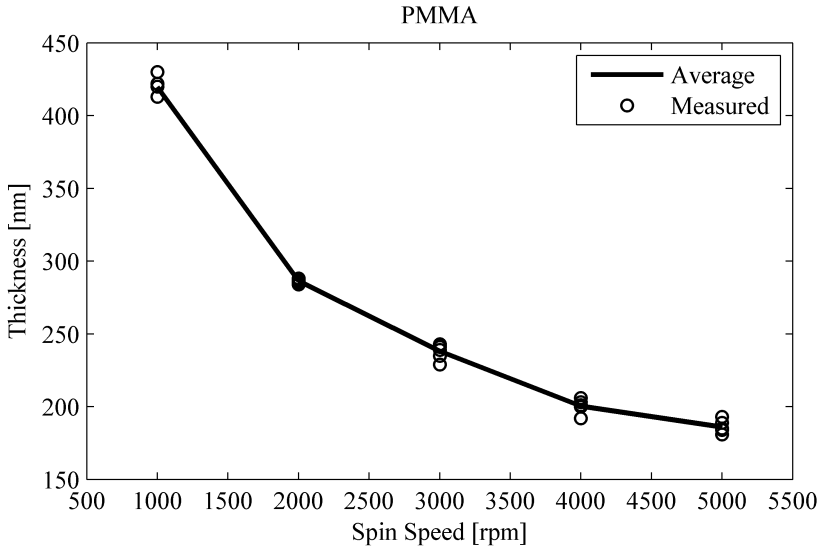

Figure 7.5: PMMA (3% solution) layer thickness as a function of spin speed. All samples were produced using a spin time duration of 1 minute. From [5].

a more uniform resist without reducing the layer thickness.
For this purpose a number of new tests were made—this time using a 4.5% PMMA solution in order to yield thicker resist layers at higher spin-speeds. The samples were examined using a profiler and the resulting data are presented in Figure 7.6. Consulting these data, it was found that a resist layer with a thickness close to

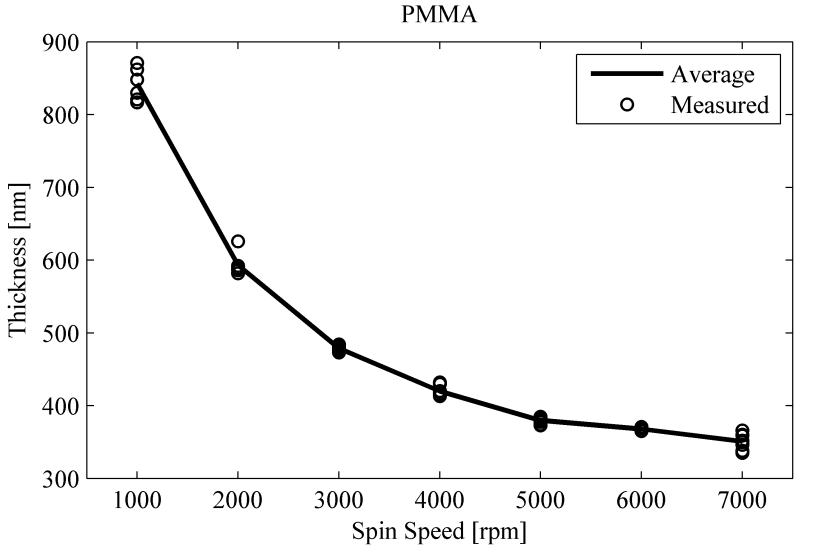

Figure 7.6: PMMA (4.5% solution) layer thickness as a function of spin speed. All samples were produced using a spin time duration of 1 minute.

400 nm was obtained when a sample was spun at 5000 rpm for 1 minute.
The procedure used when covering the wafers with PMMA was thus as follows: The wafer was cleaned in acetone in an ultrasonic bath for 1 minute. It was subsequently rinsed with ethanol and dried with compressed air before it was placed in

the spin coater. The wafer was covered in a 4.5% 950 PMMA C resist and spun at 5000 rpm for 1 minute. After deposition of the PMMA layer, the wafer was soft-baked on a hotplate at 180 °C for 90 seconds. Following the baking, the sample was ready for e-beam writing.

7.3 E-beam Writing

Before the writing of structures could be commenced, the scanning electron microscope (SEM), Zeiss model EVO 60, in combination with an external writing system, Raith Elphy Plus, should be calibrated and needed settings had to be determined. The need for and character of these steps are clarified in the following. For a start, a sample, a Faraday cup, and a wafer with structures in known dimensions are loaded into the vacuum chamber of the SEM.
The time required for proper exposure of the photo resist depends on the e-beam current—that is, the amount of electrons emitted from the electron gun. As a consequence, a rather constant current is required which is adjusted using the installed software. Next, the size of the e-beam current is needed in order to calculate the exposure time. This current is found by directing the stream of electrons into the Faraday cup such that no electrons are backscattered. The current is then measured using the built-in ammeter. A typical current used was 135 pA.
In order to write structures that properly resembles the used template, the write field of the system has to be calibrated. The write field is the area over which the system is capable of scanning at a certain magnification. So for each template that requires a different size write field, this alignment has to be carried out. The alignment is carried out by use of the sample with known structures. A predefined script is usually run where an image of the structure is taken at the desired magnification, subsequently points on the image at certain coordinates are proposed by the software after which the user—if needed corrects these points so the proposed coordinates are in agreement with the known structure. After this, the software makes a correction so small discrepancies in the lens system are compensated for. However, this alignment function was corrupt and the corrections had to be implemented manually after visual inspection of the aforementioned sample and some of the subsequently produced lithographic writings in a trial and error process.
If desired, the stage holding the sample can be rotated or a software correction can be made if the written structures are wanted at specific coordinates relative to the sample. An area of approximately 2 mm$\times$2 mm covered with the grating pattern is desired. In prior experience with e-beam writing it was found that a write field of 100 μm$\times$100 μm was well suited for writing structures with the needed resolution. Obviously, when a 2 mm$\times$2 mm area is wanted, it is required that several writings are stitched together. Because of this, the software correction is out of the question since this only acts on the global settings, i.e. the write field is not rotated accordingly, and the pieces of grating would not be in alignment with each other. Thus, the sample was rotated in order to align the written pattern with the edges of the sample. Furthermore, another alignment concerning height adjustment is done. This is required in order to retain focus on all points on the sample even though the

sample is not placed completely horizontal. At three arbitrary points on the sample, the wanted working distance is set and the height of the stage is adjusted until the sample is in focus. The XYZ positions of the stage are loaded into the software along with corresponding UVW coordinates of the writing system and the system then corrects for the skewness of the sample.
Before structures can be written with a fair possibility of success, a so-called dose test is performed. Earlier it was stated that the size of the e-beam current is needed in order to determine the proper degree of exposure. Another factor is of course the thickness of the photo resist layer. There is no way to know exactly how large a dose is required for proper exposure, so a trial and error process is carried out where templates simply are written using different doses and the resulting structures are inspected in order to decide the correct one. A silicon wafer with PMMA deposited using the previously mentioned settings was subjected to writing of these templates. After the writing had finished, the structures were developed for 30 seconds in a solution containing one part methylisobutylketone (MIBK) and three parts isopropanol (IPA), followed by 15 seconds in pure IPA in order to stop the development process. Furthermore, a thin layer of gold was sputtered onto the sample before inspection in the SEM. Some of the resulting structures can be seen in Figure 7.7. From the SEM images, it was thought that a dose factor of 1 did not suffice as the text was underexposed. With a dose factor of 1.5 and 2, all text was visible as well were areas with 50% and 200% exposure in fine condition. Higher exposures resulted in rounding of the corners which indicated overexposure. At even higher dose factors rounding of corners became more and more evident and even in the most exposed areas cross linking of the polymer occured. From these images, the best dose factor was thus found to be around 1.5 to 2. A template for the grating pattern was made—this is illustrated in Figure 7.8. Another dose test was made using this pattern and with doses ranging from 1.5 to 2 times the normal dose. All of these dose factors turned out to be too high and thus deemed inappropriate since all which was seen in the microscope was 100 μm$\times$100 μm areas stripped from e-beam resist. Another dose test with doses ranging from 1 to 1.5 times the normal dose was made. In the lower part of the interval some of the pattern was visible but in the high end of the interval all resist was removed. The dose tests shown in Figure 7.7 were so-called area dose tests and thus only suitable for determining the correct dose for writing of areas with a similar magnitude—therefore the observed discrepancy between the results.
Based on the previous dose tests, a series of tests spanning from 0.7 to 1.2 times the normal dose and with an interval of 0.1 times the normal dose was made. Also, in the tests already made, it was seen that the exposed areas were rotated with respect to the defined coordinates of the UVW system and furthermore that the areas overlapped at the edges. This was due to inaccuracies during the manual set-up of the write field in the alignment process, so in the tests described in the following also factors for correction of the write field was sought. In order to decide the corrections, three areas with different spacings were written both laterally and vertically for each dose. Close-up images of the resulting grating pattern stemming from different doses are shown in Figure 7.9. From the figure it is seen that a dose factor of 0.7 results in a pattern which do not resemble the template—also, the photo resist

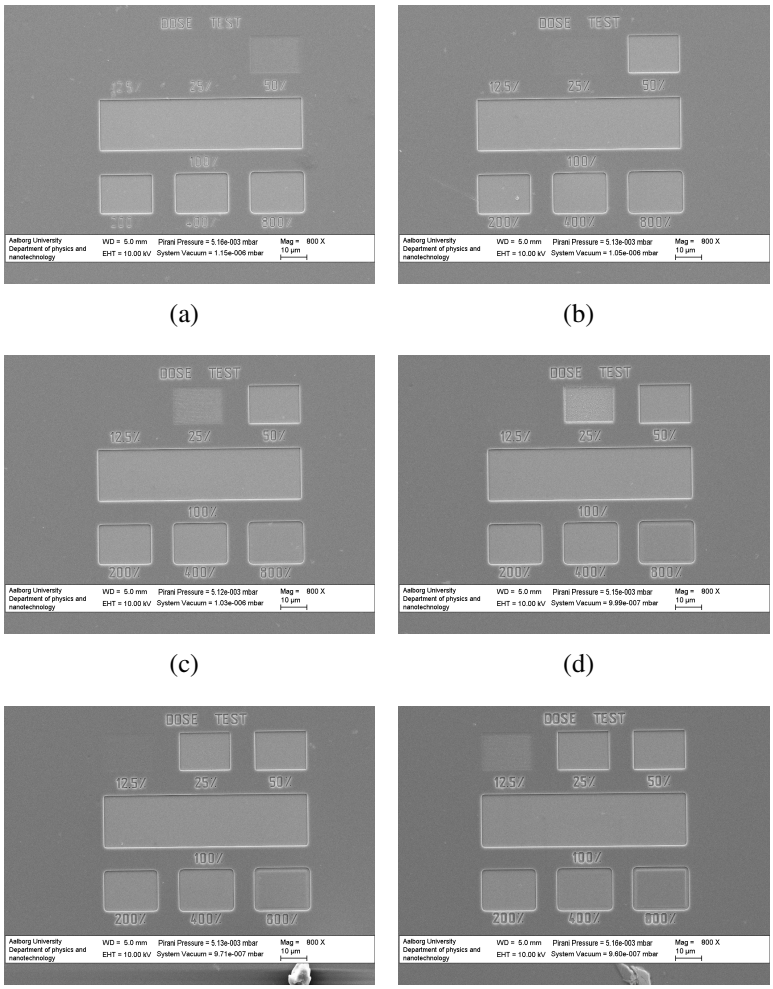

Figure 7.7: SEM images of dose tests. (a): Dose factor 1. (b): Dose factor 1.5. (c): Dose factor 2. (d): Dose factor 2.5. (e): Dose factor 3. (f): Dose factor 4.

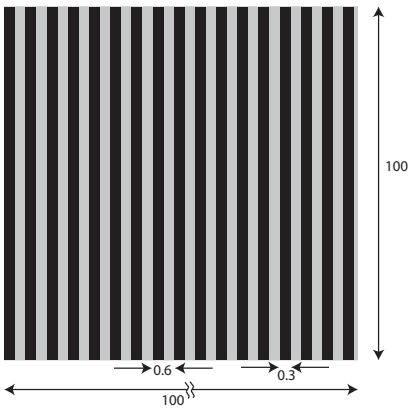

Figure 7.8: Schematic representation of the template used for e-beam writing of the grating structure on a silicon wafer. The lengths are given in microns.

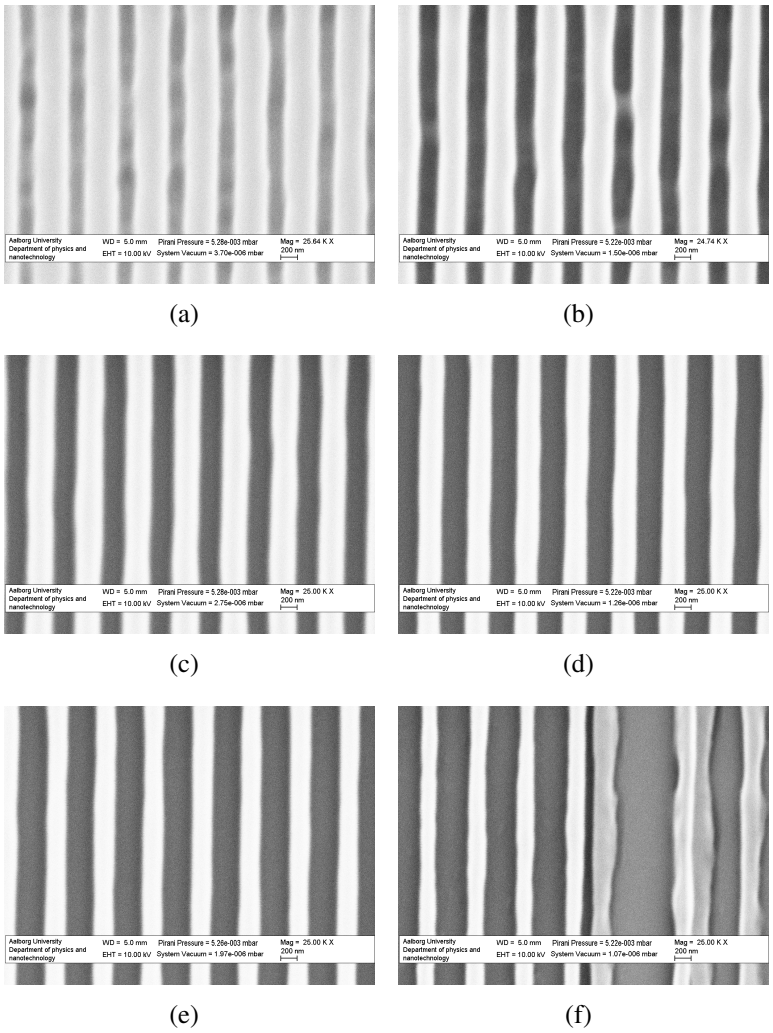

Figure 7.9: SEM images of dose tests of 600 nm gratings. (a): Dose factor 0.7. (b): Dose factor 0.8. (c): Dose factor 0.9. (d): Dose factor 1.0. (e): Dose factor 1.1. (f): Dose factor 1.2.

is not developed all the way through to the silicon wafer—clearly an underexposed situation. A dose factor of 0.8 still results in rather pronounced underexposure. A dose factor of 0.9 yields a slightly underexposed grating. A dose factor of 1.0 shows the best result—the result is as desired with a period of 600 nm and a structural width of approximately 300 nm. Higher dose factors result in overexposure where too much of the e-beam resist is removed and ultimately—even collapses of the pattern are evident. Based on these findings, a dose factor around 1.0 is found to be the best.
Unfortunately, the overall picture of the grating is quite different—a gradient in the degree of exposure is seen in all of the writings—cf. Figure 7.10. Additional tests has been made in order to clarify if the phenomenon persisted. A single test showed other tendencies (more about this later), but all other tests before and after that one showed the phenomenon.
Furthermore, another problem became visible. The patterns which were repeated

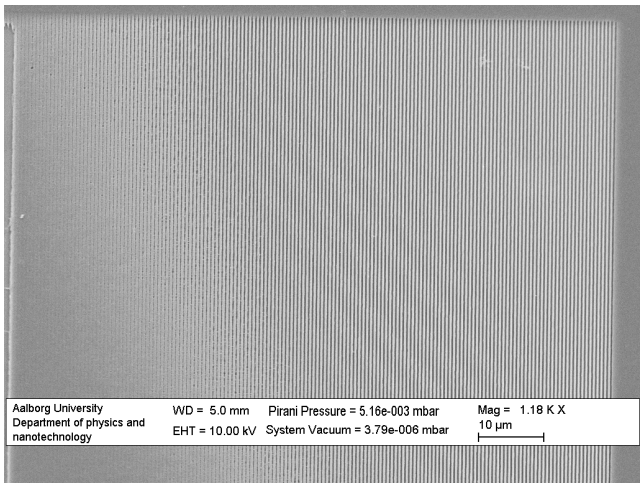

Figure 7.10: Captured image of a written grating which shows the all-time present gradient in the degree of exposure.

laterally were written first and subsequently the patterns which were repeated vertically were written. From the developed structures it was clear that the needed dose for proper exposure changed during the writing process, cf. Figure 7.11. The rows

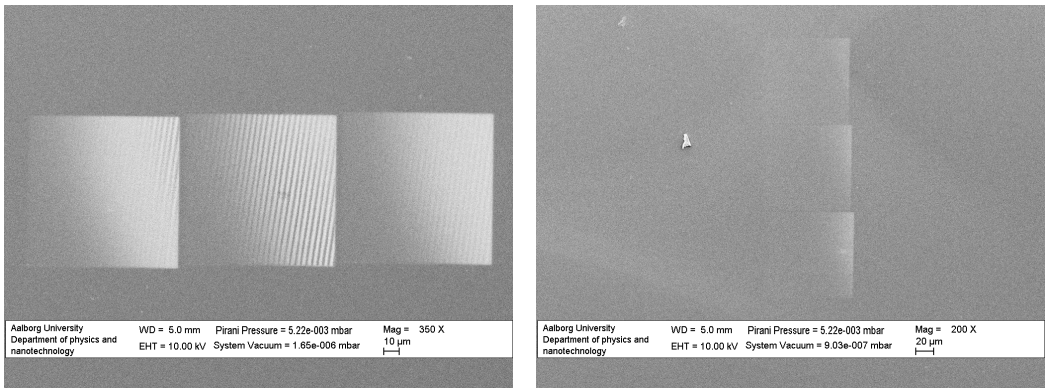

(a) (b)

Figure 7.11: SEM images of what should have been gratings with structures of 300 nm width. The structures in both images are written with a dose factor of 0.8.

with the laterally and vertically directed repetitions both show the same tendency of increased exposure corresponding to an increase in dose factor. However, writings done with the same dose factor are not exposed to the same degree. This was believed to be due to a non-constant e-beam current which was altered over time or an uneven distribution of e-beam resist across the silicon wafer. This problem was sought clarified in the test described in the following.
Again, another dose test was performed—this time ranging from 0.9 to 1.1 times the normal dose but with an interval of 0.5 times the normal dose. An overview of the resulting structures is seen in Figure 7.12. All the structures which are seen repeated laterally were written first and subsequent all the vertically repeated structures were exposed—from left to right. The structures are paired up two and two—written with

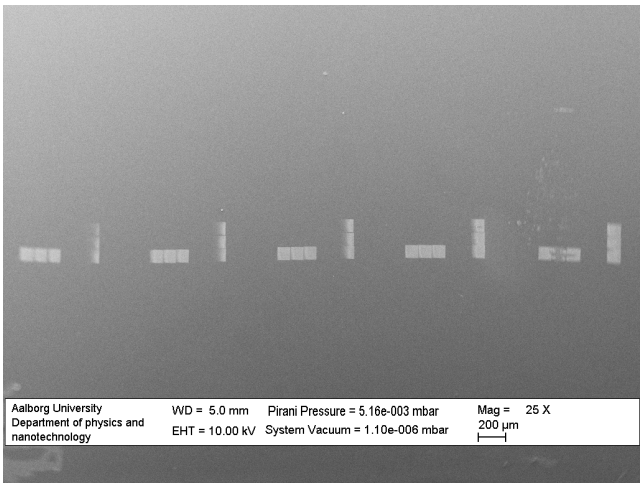

Figure 7.12: Overview of the written structures where a time related change in exposure is observed.

the same dose factor. This clearly indicates that the difference in exposure is independent of the place in where it is written and that it must be because of a change in the e-beam current which happens over time. A dose factor of 1.1 is clearly too much but locally the rest of the dose factors yield similar and better results. Due to the still persisting exposure gradient (cf. Figure 7.13) nothing more accurate can be said at this time.

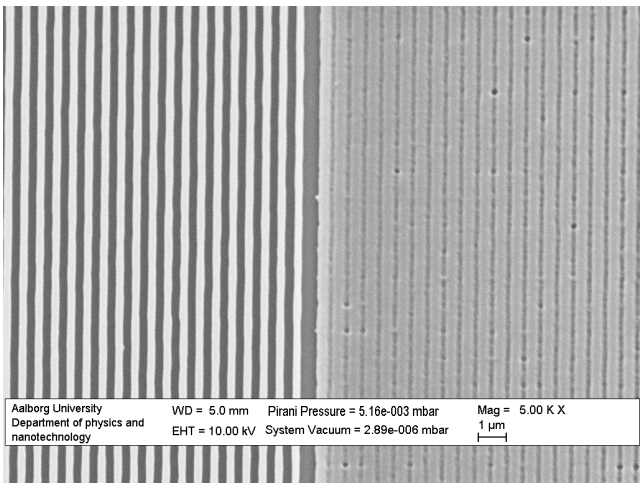

Figure 7.13: Transition from one exposed area to the next where the gradient in exposure is observed.

After this, new settings for the correction to the write field were used without deliberately changing any other conditions than the e-beam current. In contrast to previously obtained results, a rather uniform exposure is observed in the images presented in Figure 7.14. Only in the upper right corner of the written area, non-uniformity can be observed. Furthermore, the upper right corner seems underexposed as opposed to previous writings where the same corner was overexposed. By use of what is deemed to be the same settings—besides use of both old and new

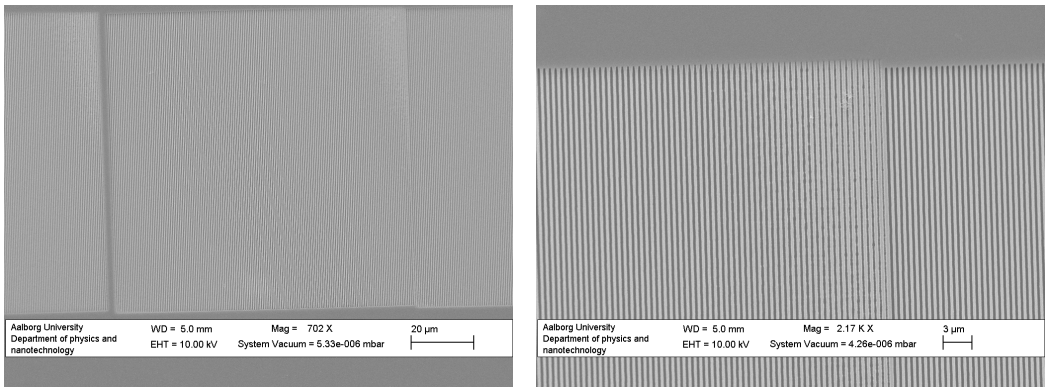

(a) (b)

Figure 7.14: SEM images of a grating structure where the previously observed gradient in exposure has nearly vanished. A dose factor of 0.9 was used for this particular writing.

settings for the write field—several attempts were made to recreate this result, but all attempts were unsuccessful. Close-up images of the resulting structures are presented in Figure 7.15. Based on the dimensions of the gratings in these images,

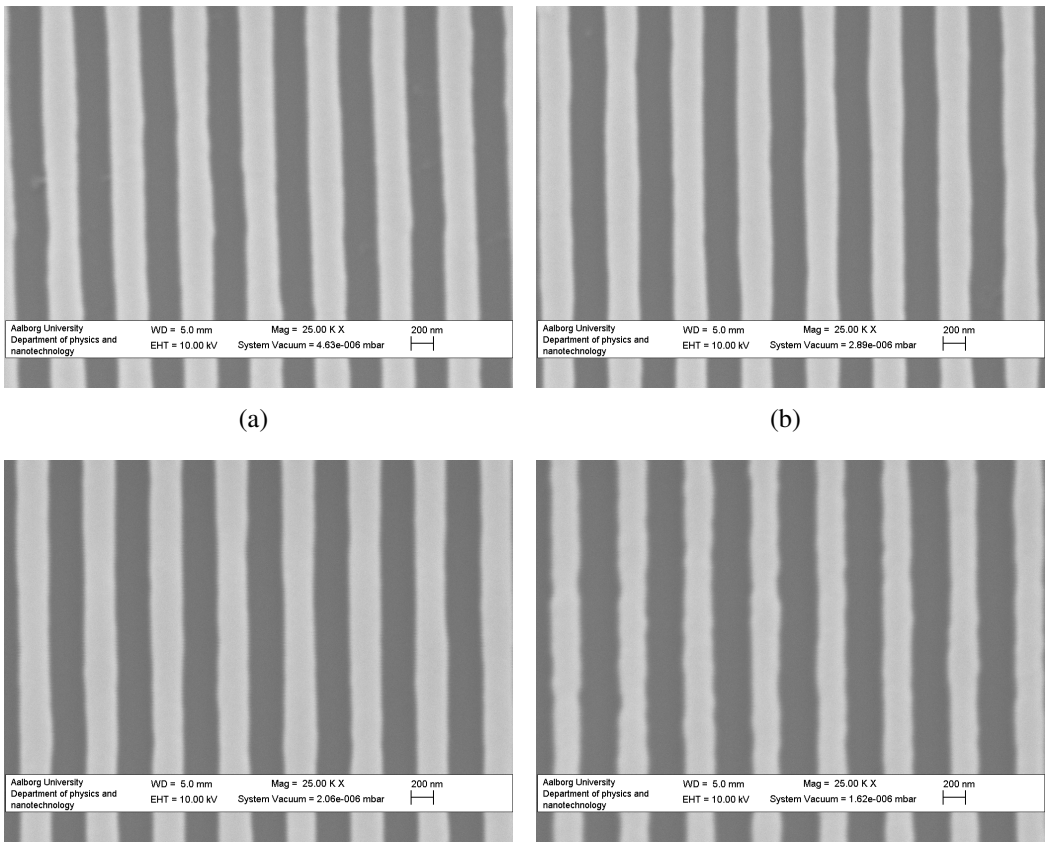

(a) (b)

(c) (d)

Figure 7.15: SEM images of dose tests of 600 nm gratings. (a): Dose factor 0.90. (b): Dose factor 0.95. (c): Dose factor 1.00. (d): Dose factor 1.05.

the best dose is determined to be 0.9 times the normal dose. This dose factor was decided to be used as the initial dose in the following attempts towards uncovering the reason behind the observed gradient in exposure.
The writing system is connected to two electron microscopes (Zeiss EVO 60 and 1540 XB) through a system of switch-boxes. Samples written using the XB electron microscope did not show the gradient in exposure (cf. Figure 7.16). The EVO

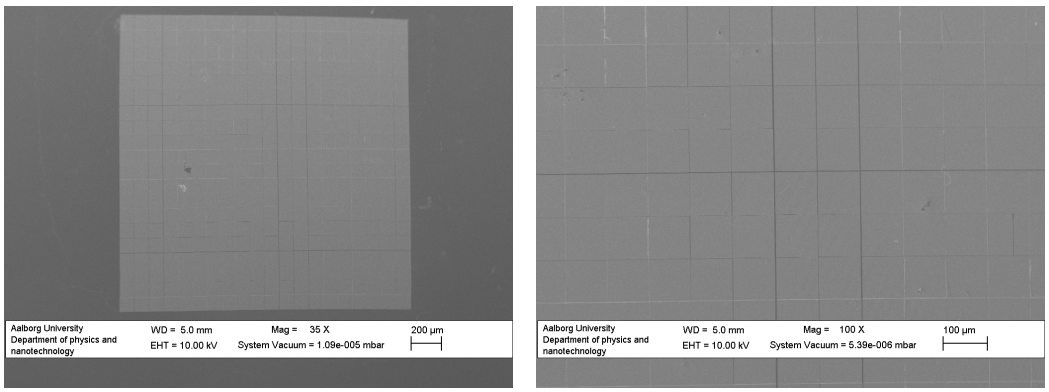

(a) (b)

Figure 7.16: SEM images of a grating structure written using the XB electron microscope. No gradient in exposure is observed.

60 electron microscope used for the writing of the samples showing the gradient was placed farther away from the writing system than the XB microscope and to rule out bad connections or signal quality loss through the relatively long cables and wires, the writing system was connected directly to the EVO 60 electron microscope. Three different samples were written with this hardware setup and all samples still showed the gradient, after which the setup was changed back to its original configuration. Another hypothesis was investigated. It was believed that the gradient in exposure could be due to charging of the sample-wafers and steps were hereafter taken in order to solve this problem. These attempts are described in the following.

7.3.1 Doped Wafers

If indeed the wafers were charged by the stream of electrons, the problem could be solved by leading the electrons away more readily. It was investigated if higher conductivity of the wafers could counteract the observed gradient and so a number of writings on doped silicon wafers were done. As seen from the examples on some of the writings in Figure 7.17, the gradient is persistent. As no improvement was noted—subsequently, ordinary silicon wafers were used for the writings.

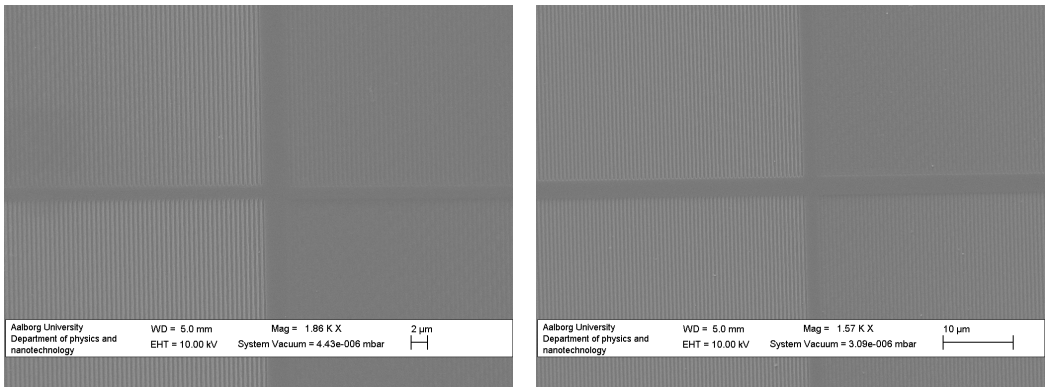

(a) (b)

Figure 7.17: SEM images of writings of gratings on doped silicon wafers.

7.3.2 Exchange of Sample Holder

Increasing the conductivity of the sample did not work. The wafers were attached to the sample holder by use of conducting carbon tape. In order to confirm or rule out that the possible charging of the wafer was due to poor contact between the wafer and sample holder, another sample holder was used instead. This sample holder was primarily used in the XB microscope which thus also might explain why that microscope yielded better results. When using this sample holder, the wafers were placed directly on the holder and held in place by screws.
The results from this change showed clear improvements. The gradient was still visible, but not as distinct as in the case of previous writings. It was decided to use this sample holder from this point and on. A few writings were again performed with the use of doped wafers. This was done in order to investigate if the combined effect of increased conductivity between the sample holder and sample and in the sample itself would yield further improvements. Again, the use of doped wafers did not improve the situation further.

7.3.3 Reduced Resist Thickness

Following the improvements in conductivity, numerous writings were done where different smaller resist thickness's were used. The reason for this was, that when an uneven exposure is noted, the difference in exposure results in smaller overall deviations at small resist thickness's than for large thickness's. Furthermore, a lower electron dose is required which also may result in lesser charging of the wafer. Rather good results were seen from wafers covered with $\approx$100 nm e-beam resist, but this resist thickness was deemed too low for the intended use of the written structure. At a resist thickness of $\approx$225 nm a compromise was made. A useful resist thickness had been reached, but the trade-off was an increased difference in exposure across the write field. The result is seen in Figure 7.18. As may be seen from Figure 7.18 (a), the difference in exposure is most clear in the bottom-left and top-right corners. It was decided to try to make use of only a part of the write field.

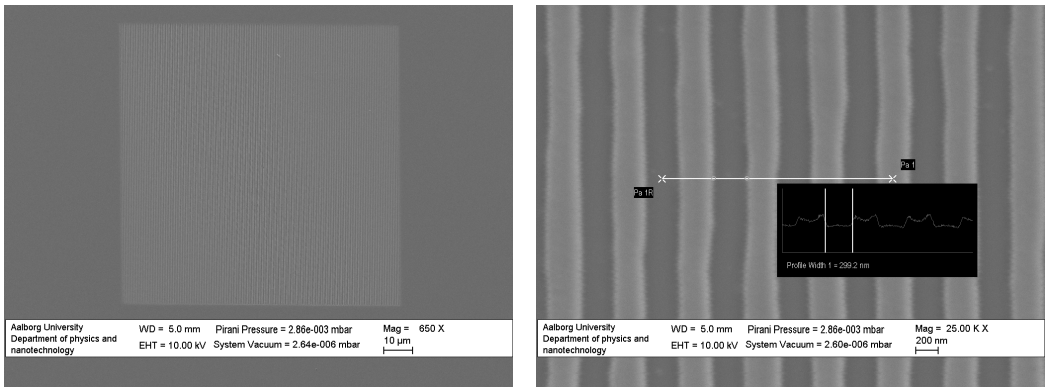

(a) (b)

Figure 7.18: SEM images of writing done on a wafer covered with 225 nm e-beam resist.

An area of 50 μm$\times$50 μm was written using the 100 μm$\times$100 μm write field and the result was far better than before even though the gradient in exposure was still visible (cf. Figure 7.19). Based on this, it was decided that a rather uniform grating

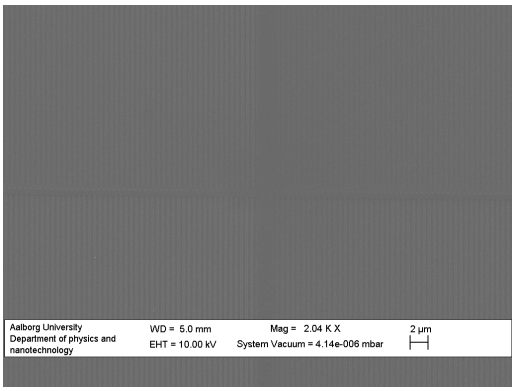

Figure 7.19: 50 μm$\times$50 μm areas stitched together. The gradient in exposure is still discernible.

could be made. Again, of course there was a trade-off. First, the periodicity of the over-all grating would be broken more often, due to the increased number of areas stitched together. Second, the time used to write the desired area was increased significantly. This was also due to the increased number of area elements which demanded a four-fold increase in stage operations.

7.3.4 Altered Electron Energy

It is seen from Figure 7.18 (b), that the resulting lines are not entirely straight. The quality of the exposure could possibly increase with the electron energy in the sense that the edges of the lines would become more sharp. The energy of the electrons was therefore increased by changing the high-tension from 10 kV to 30 kV. One of the results can be seen in Figure 7.20. It is seen that the frequency of the variations along the written pattern have been increased compared to the situation before. The

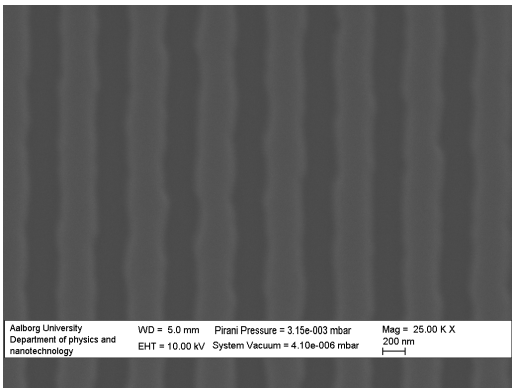

Figure 7.20: Grating structure written with electrons accelerated by 30 kV instead of 10 kV which was previously used.

quality of the structure itself has not been improved as expected. Once again there is a trade-off for the change in parameters. The exposure of the e-beam resist is done by secondary electrons. Due to the increased energy of the electrons, they penetrate deeper into the material and into the silicon wafer why the creation of secondary electrons in the resist is decreased and as a consequence a higher dosage of electrons is needed. This of course again results in increased exposure time and a more time consuming production. In this instance, it was decided that the change from 10 kV to 30 kV in high-tension was not worth the trade-off and the operation of the microscope was resumed with an EHT of only 10 kV.

7.4 Gold Gratings

After a dose-test where an appropriate exposure time was found, an area of 2 mm$\times$ 2 mm was stitched together by 50 μm$\times$50 μm areas and written on a silicon wafer covered with 225 nm PMMA. The pattern was developed by placing the sample in a one part methylisobutylketone (MIBK) and three parts isopropanol (IPA) solution for 30 seconds and subsequently in an isopropanol solution for 15 seconds. The sample was loaded into the vacuum chamber of a Cryofox 600 Explorer and $\approx$60 nm gold was evaporated onto the sample through e-beam evaporation. Following this, lift-off was performed, where the sample was placed in acetone for half an hour and placed in an ultra-sonic bath for $\approx$30 seconds at the lowest power setting. The result is seen in Figure 7.21. First, it is seen that the sample was not 2 mm$\times$2 mm large. The reason for this was that the filament which provided the electrons broke during the e-beam writing process. It is also seen that the lift-off process was not a total success. From Figure 7.21 (b) it seems that the exposure of the grating pattern was not carried out all the way through to the silicon wafer and as a result the gold wires are not entirely attached to the silicon surface. In many cases, it also seems that the wires which were not fully attached were torn off across the entire write field.
It was thus found that the electron dosage was not large enough to obtain a descent grating. At the same time the dosage was locally too large to obtain the desired 300 nm wide gold wires (cf. Figure 7.22). Based on these findings it was decided to

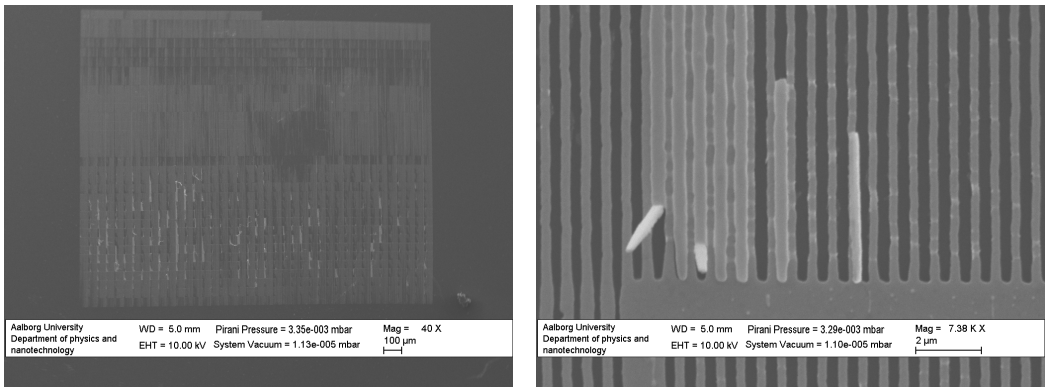

(a) (b)

Figure 7.21: (a) Overview of a grating comprised of 50 μm$\times$50 μm areas onto which gold has been evaporated and lift-off has subsequently been sought performed (the electron source filament broke during the e-beam writing process). (b) Zoom-in on the lower-left corner of one of the 50 μm$\times$50 μm areas.

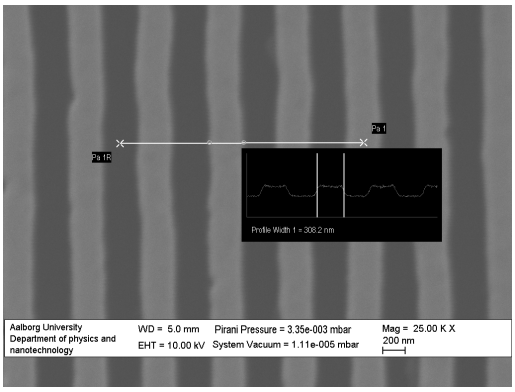

Figure 7.22: Close-up of some gold wires from the sample depicted in Figure 7.21.

maintain the period of the grating structure but increase the width of the gold wires and in that way obtain a proper gold grating. A dose-test was performed where the sample was taken through the entire procedure as described in the beginning of this section to ensure that it was possible to do a proper lift-off. Following this, a number of samples were written with different electron dosages to obtain different wire widths and again the procedure outlined previously was followed for all samples. As the making of 300 nm wide wires is discarded, 100 μm$\times$100 μm write fields are used instead in order to speed up the process. The resulting 1 mm$\times$1 mm gratings are presented in Figures 7.23 to 7.27. The width of the gold wires was found to vary a little across the gratings—typically 5–10 nm's. The values given in Figures 7.23 to 7.27 are thus approximate values found in the middle of the observed interval. Except from Sample *E* in Figure 7.27, the gratings are all deemed successful. Few flaws are observed and the gratings seem homogeneous across the written areas. Sample *E* on the other hand is seen to have serious flaws. The reason for this is believed to be cross-linking of the e-beam resist which thus cannot be removed in the developing process. Again, the gold is not properly attached to the

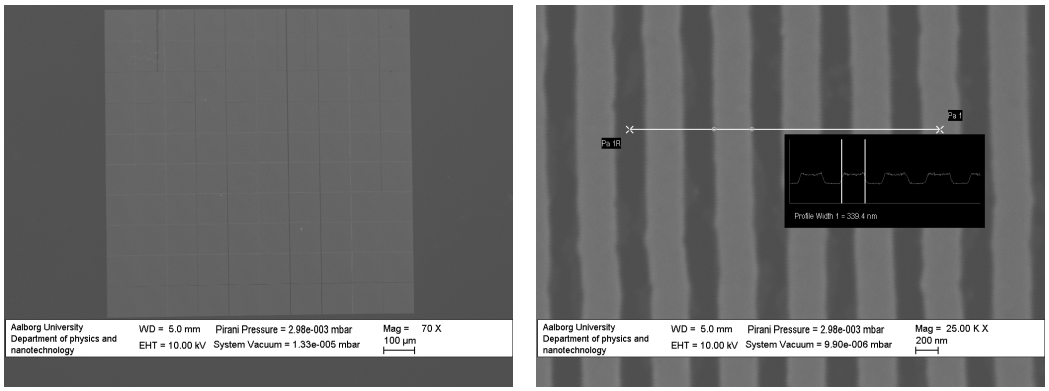

(a) (b)

Figure 7.23: (a) Grating overview of Sample *A*. (b) The width of the gold wires is found to be ≈340 nm.

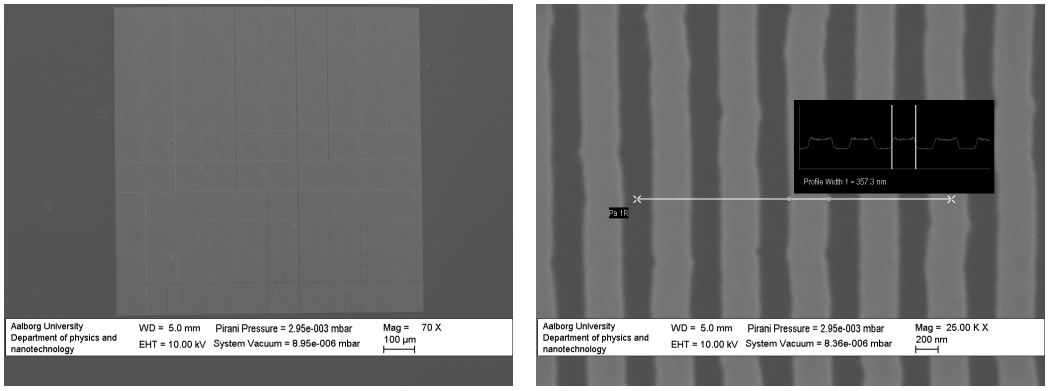

(a) (b)

Figure 7.24: (a) Grating overview of Sample *B*. (b) The width of the gold wires is found to be ≈350 nm.

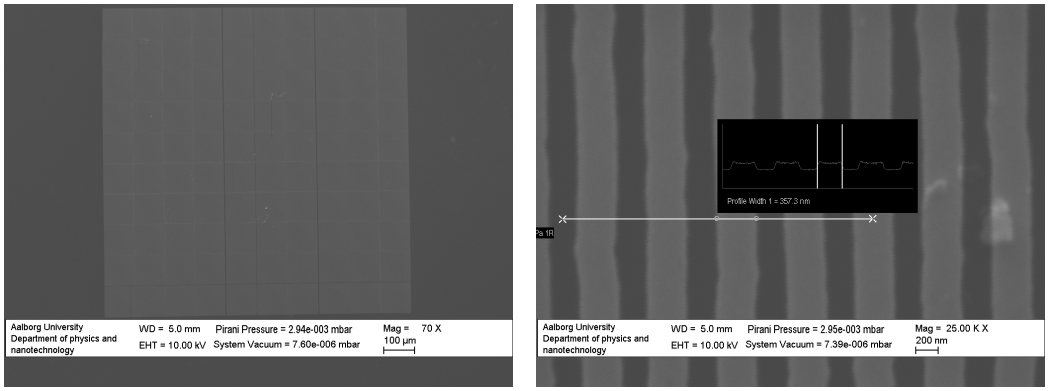

(a) (b)

Figure 7.25: (a) Grating overview of Sample *C*. (b) The width of the gold wires is found to be ≈355 nm.

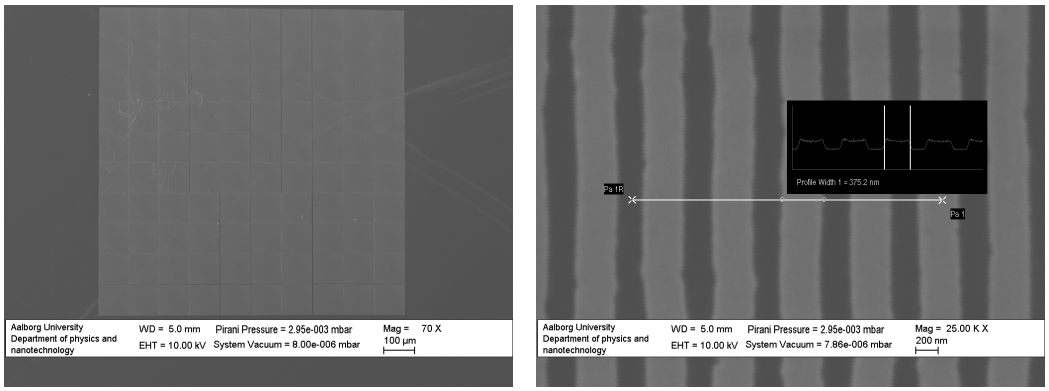

(a) (b)

Figure 7.26: (a) Grating overview of Sample *D*. (b) The width of the gold wires is found to be ≈375 nm.

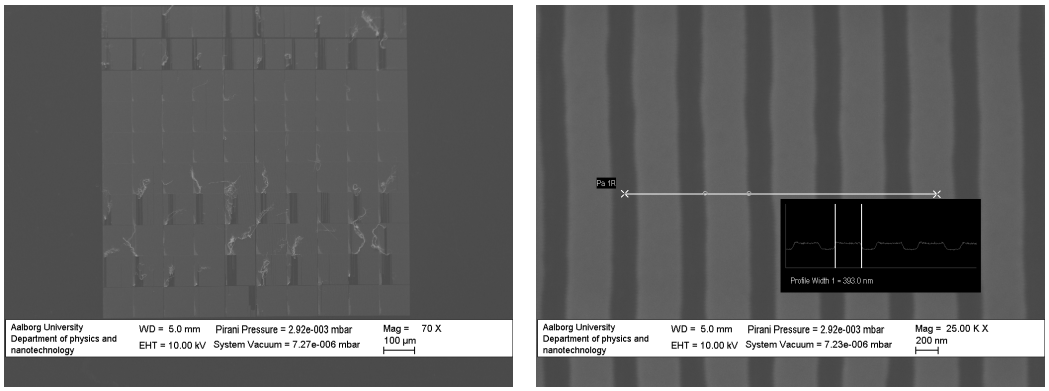

(a) (b)

Figure 7.27: (a) Grating overview of Sample *E*. (b) The width of the gold wires is found to be ≈390 nm.

silicon surface and the wires are stripped from the wafer in the lift-off process. Later, it turned out that it was very difficult to properly focus the laser beam on the samples during the measurements and as a consequence a larger area was written by use of the XB electron microscope. The resulting grating is depicted in Figure 7.28. It is seen that the quality of the resulting grating is far better than on the other samples. The gold wires are seen to be almost straight and not uneven as compared to previous samples. Finally, the width of the wires is more constant—again compared to Samples *A* to *E*. Sample *F* was also characterised in an atomic force microscope (AFM) in order to obtain height information. From Figure 7.29 it is seen that the width of the wires is consistent with that found by use of the scanning electron microscope. The height is ≈63 nm and the profile is seen to have tilted edges and not vertical as expected. This may be due to the shape of the cantilever tip of the AFM which keeps the tip away from precisely following the shape of the wires.

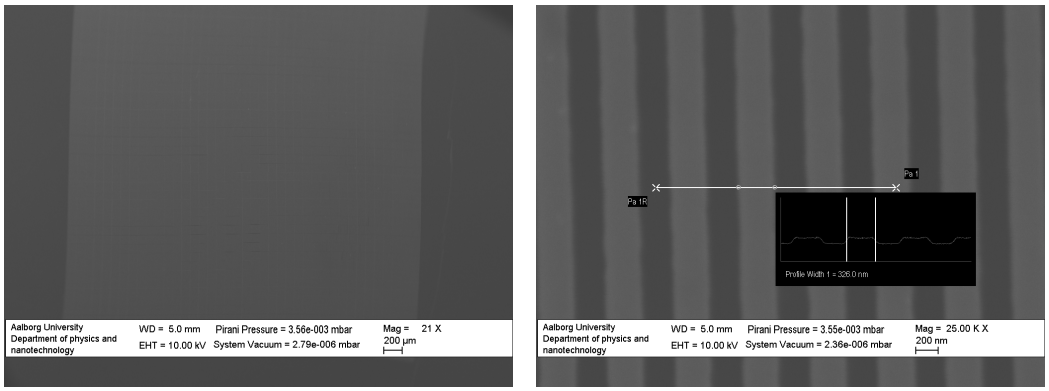

(a) (b)

Figure 7.28: (a) Grating overview of Sample *F*. The e-beam writing was done on the XB microscope. (b) The width of the gold wires is found to be ≈325 nm.

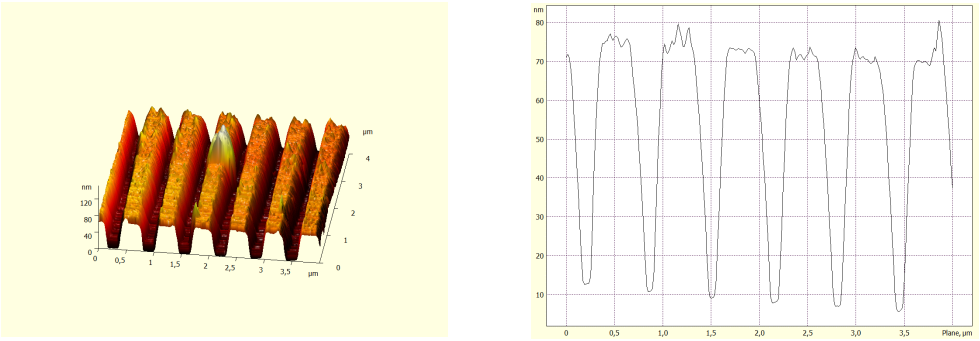

(a) (b)

Figure 7.29: (a) AFM image of Sample *F*. (b) The height of the gold wires is found to be 60 nm–65 nm.

7.5 Silicon Gratings

The important aspect of this project was to characterise gold gratings. However, in order to interpret the spectra obtained from optical measurements, it was thought fruitful also to obtain spectra from silicon gratings. The making of these gratings started out much in the same way as the gold gratings. Several dose-tests were made and 1 mm$\times$1 mm areas were written with different doses and subsequent developed. The samples were etched through reactive ion etching (RIE) and the surplus PMMA was removed with acetone. The samples were etched for 40 seconds in a mixed 15 sccm SF_6 and 5 sccm O_2 gas flow at a pressure of 35 mTorr, using a power of 50 W. The resulting gratings are seen in Figures 7.30 to 7.32. Sample *H* is seen to be the most flawed. One would expect Sample *I* to be the most flawed since the width of the silicon tops is largest in this case—corresponding to the least exposed sample in the e-beam writing process. Sample *H* is in fact the least exposed sample—which explains the non-etched corners of the write field areas. The reason for the smaller wire width is believed to stem from the etching process. Even though

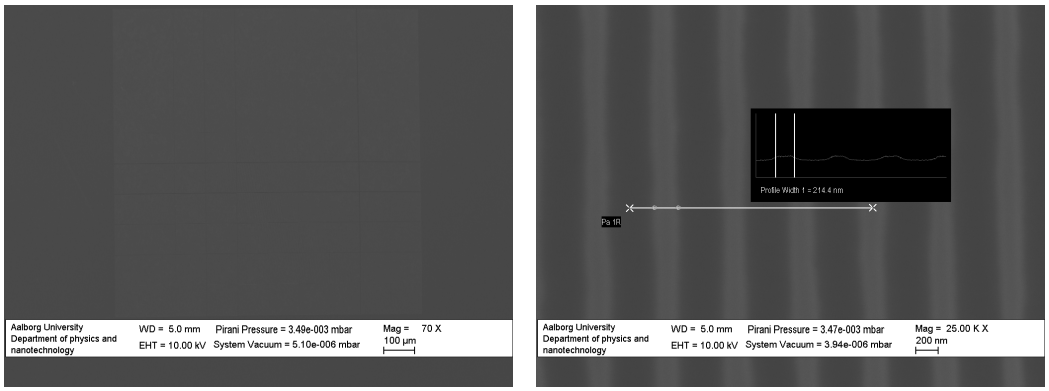

(a) (b)

Figure 7.30: (a) Grating overview of Sample *G*. (b) The width of the silicon wires is found to be ≈210 nm.

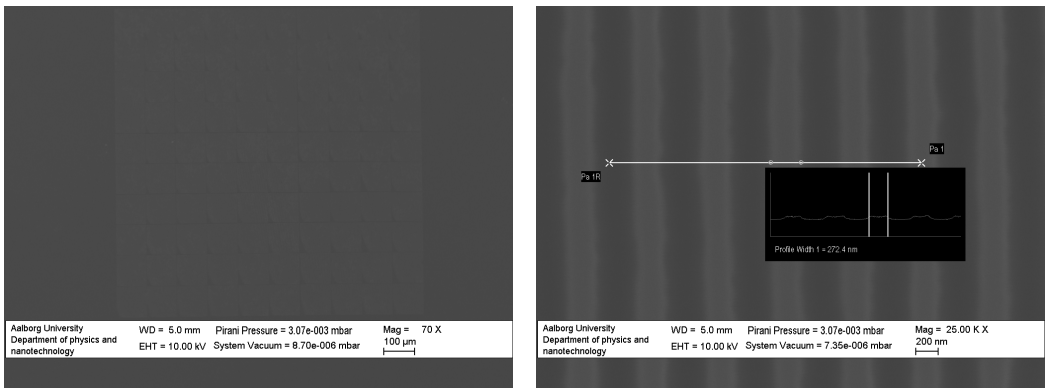

(a) (b)

Figure 7.31: (a) Grating overview of Sample *H*. (b) The width of the silicon wires is found to be ≈270 nm.

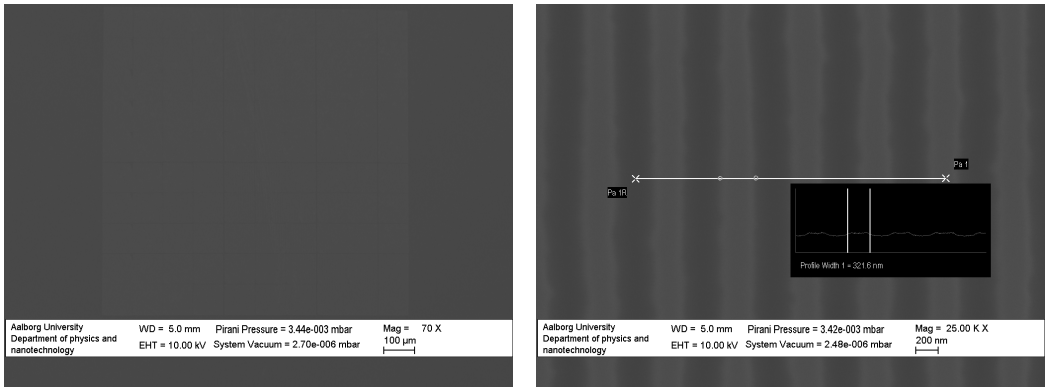

(a) (b)

Figure 7.32: (a) Grating overview of Sample *I*. (b) The width of the silicon wires is found to be ≈320 nm.

suitable parameters for a stable etching is sought—sometimes the etching halts for a small period of time. It is thought that Sample *H* is effectively etched for a longer period of time than Sample *I* which thus explains the discrepancies between the written masks and the resulting gratings.
Using the XB microscope, also in this case a grating with a larger area was made. The resulting grating can be seen in Figure 7.33. It is seen that the entire area

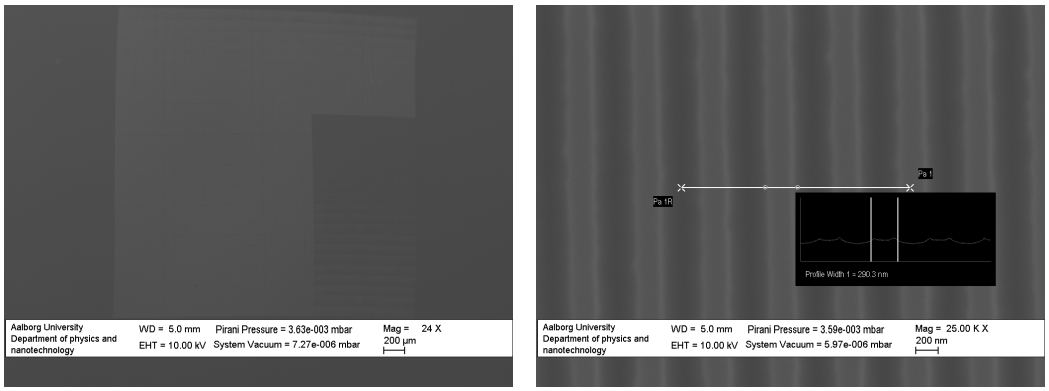

(a) (b)

Figure 7.33: (a) Grating overview of Sample *J*. (b) The width of the silicon wires is found to be ≈290 nm.

was not exposed evenly and as a result the etching is also uneven. However, an area large enough to do proper measurements on was successfully made. Sample J was also characterised through use of an AFM (cf. Figure 7.34). The observed

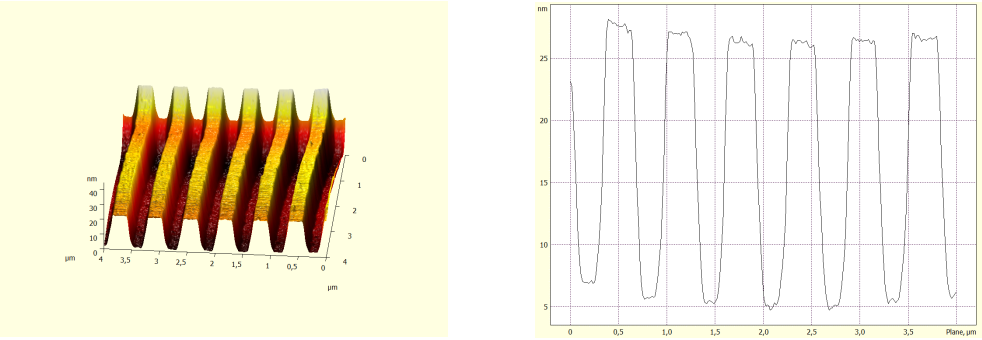

(a) (b)

Figure 7.34: (a) AFM image of Sample *J*. (b) The height of the silicon wires is found to be ≈22 nm.

height of 22 nm of the wires are quite small in comparison to what was expected. Through previous etchings the height was found to be in the range of a few hundred nm's. The reason for this may be that the e-beam resist was not exposed all the way through to the wafer and that an amount of resist had to be etched away first. Furthermore it is seen that the FWHM is consistent with the findings from the SEM images.

Optical Measurements

8

In Chapter 3 it was found that enhanced electrical fields may form if the plasmon resonance frequency of the material is hit. Furthermore, it was found that scattered fields could supply a momentum component to the impinging electrical field and the criteria for surface plasmon polaritons could thus be fulfilled. In Chapter 6 it was mentioned that second harmonic spectroscopy is extremely surface sensitive and that strong fields are required to achieve a strong response. Second harmonic spectroscopy is therefore chosen as an indirect characterisation method for investigating enhanced near-fields in the grating structure.
The experimental setup is illustrated in Figure 8.1. A pulsed 10 MHz signal with

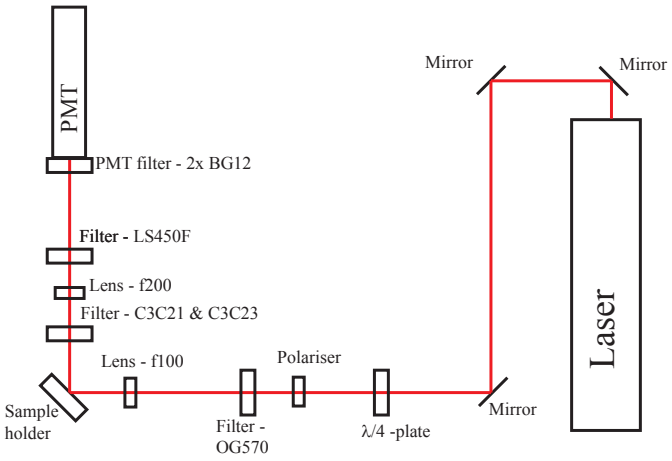

Figure 8.1: Illustration of the experimental setup in connection with the measurements of the second harmonic response from the produced samples.

a wavelength of ≈786 nm from a Tsunami laser was lead through a quarter-wave plate which altered the signal from linear polarisation to elliptical polarisation. In this way the following polariser could be used to decide if the probing signal should be *p*- or *s*-polarised. Furthermore, the intensity of the signal could be adjusted by use of the quarter-wave plate. The signal was then carried through a filter which filtered away wavelengths below 570 nm such that a contribution from the pumping signal to the measured second harmonic signal was avoided. The signal was then focused onto the sample which was placed in the sample holder. The sample holder could be rotated 360 degrees by use of a stepping motor. The response signal from the sample was lead through a series of filters which filtered away the pumping

signal and through a second lens which focused the second harmonic signal onto a photo multiplier tube (PMT) with which the second harmonic response was measured.

The impinging electromagnetic field was either *p*- or *s*-polarised and the plane of incidence was perpendicular to the wires constituting the gratings at the 0 degrees position (cf. Figure 8.2). The wavelength of the incident field was 785 nm–787 nm

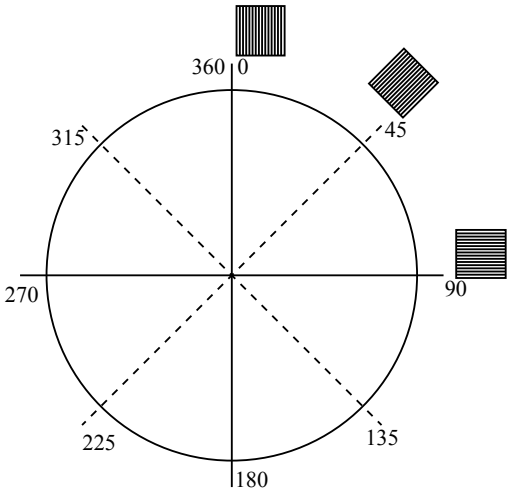

Figure 8.2: Illustration of the sample orientation compared to the corresponding angle in the following results.

(a slight shift in wavelength occurred during the measurements). A reference measurement was made on the bare silicon of the different samples. This was done in order to compensate for skewness occurring when the sample was placed in the sample holder. Due to the skewness, the reflected signal would hit the PMT uneven as the sample was rotated. Figure 8.3 shows a plot of raw data and a plot of the data with reference correction. The correction of the different data points of the measurements was done by dividing the data values with the corresponding value of the reference measurement and multiplying with the average value of the reference data-set. Figure 8.4 shows the second harmonic spectra from a gold grating—namely Sample *F*. The gratings were made on Si(100) wafers. The Si(100) interfaces have non-vanishing susceptibility tensor elements which result in an isotropic second harmonic response during azimuthal rotation as is the case in these experiments. There is also an anisotropic bulk contribution from the silicon which arises due to a quadrupole-type non-linearity [4]. This contribution is, however, deemed negligible in this context.
Different mechanisms are thought to be responsible for the observed response. First, the responses at 0 degrees and 90 degrees are compared. At 90 degrees the *p*-polarised incoming field has a field component perpendicular to the wafer and a component along the wire-axis. At 0 degrees the field components are perpendicular to the wafer as well as the wire-axis. Focusing on the field components perpendicular and parallel to the wire-axis, the perpendicular component experi-

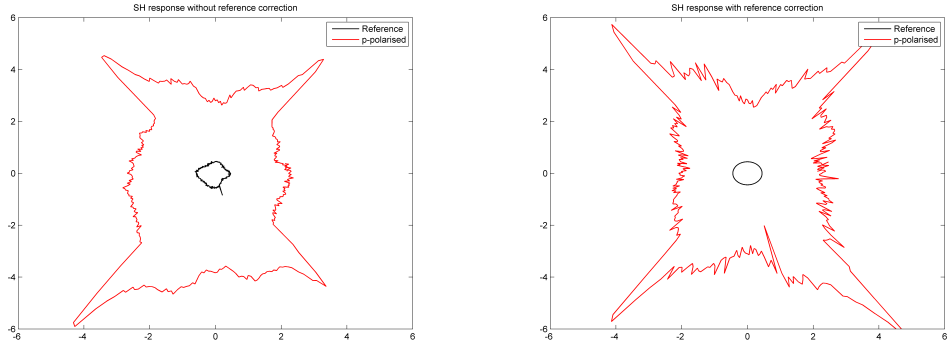

(a) (b)

Figure 8.3: Second harmonic response from a gold grating without (a) and with (b) reference correction.

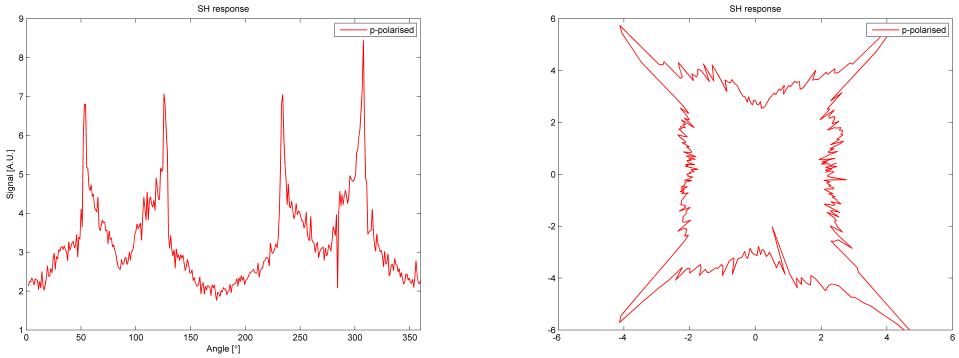

(a) (b)

Figure 8.4: SHG response from Sample *F* with ≈325 nm wide gold wires constituting a grating with a 600nm period.

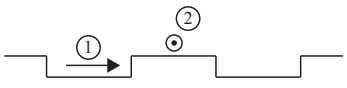

Figure 8.5: Illustration of the orientation of the electrical field components at 0 degrees and 90 degrees—marked by '1' and '2', respectively.

ences anisotropy (cf. Figure 8.5). It is thus expected that the effective second order susceptibility is larger at 0 degrees than at 90 degrees and therefore also the observed second harmonic response. By inspection of Figure 8.4 this is seen not to be the case—at least not as a dominating mechanism. Another explanation must be

sought.
The second harmonic response is also proportional to the electrical field strength squared. If Figure 8.5 again is observed, the electrical field component within the gold wire in the situation marked '2' is equal to the electrical field component of the exciting field. This is the result of the boundary condition across the interface being fulfilled. In the situation marked '1', the boundary condition implies that the normal component of the dielectric displacement has to be continuous across the interface. This results in a decrease of the field strength within the gold wire—namely by a factor $1/\varepsilon_{Au}$. If this mechanism is dominant, the largest second harmonic response is expected when the grating is rotated to 90 degrees. Again, if the second harmonic spectra from Figure 8.4 are observed, the response values at 0 degrees and 90 degrees are seen to be explained by this mechanism.
In order to solidify these explanations or prove them wrong, the polarisation of the incoming field was changed from 'p' to 's'. The result is seen in Figure 8.6. It is

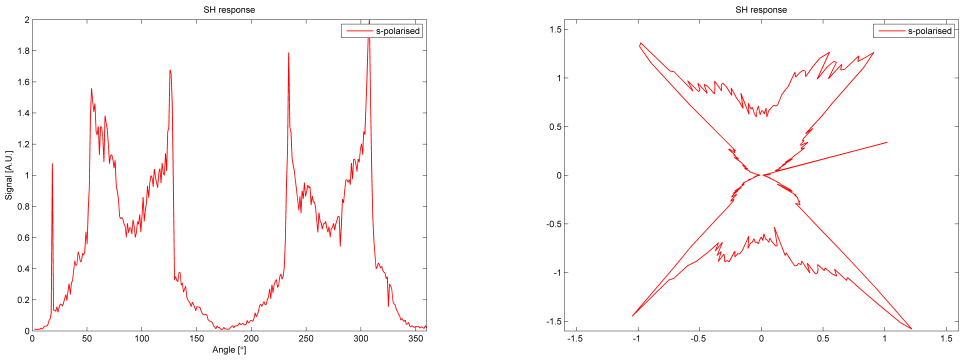

(a) (b)

Figure 8.6: SHG response from Sample F with ≈325 nm wide gold wires constituting a grating with a 600nm period.

seen that this spectrum, qualitatively, is the same as the spectrum for p-polarised excitation. Due to the 90 degrees shift in polarisation, the opposite tendency of Figure 8.4 should have been observed in Figure 8.4. The assumption concerning the shift in anisotropy may still be valid and of importance, since it is possible that the response at 90 degrees in the p-polarised case is dominated by other mechanisms.
A large response is seen at ≈52 degrees. This do not add up with the so far proposed mechanisms. The response is repeated in a symmetric fashion which renders a high probability that the response is related to the periodicity of the grating. The second harmonic response measured from Sample J is shown in Figure 8.7. In this instance, a larger response is found at 0 degrees than at 90 degrees, which indicates that the dominating reason for the response is the change in effective susceptibility due to the anisotropy of the grating—which also was the indication from the s-polarised case of Sample F. Also in this spectrum, the characteristic periodic response is present. The characteristic peaks in intensity are found at the same angles as in the spectrum for Sample F, which further indicates that the response is due to the period of the grating. The second harmonic response due to an s-polarised

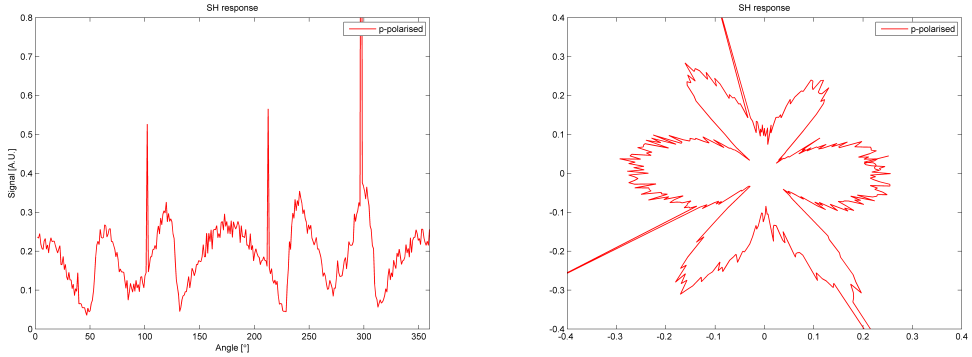

(a) (b)

Figure 8.7: SHG response from Sample *J* with ≈290 nm wide silicon wires constituting a grating with a 600nm period.

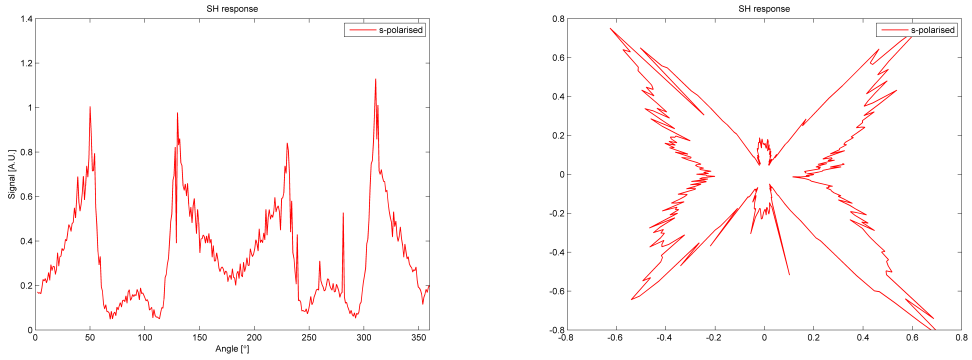

(a) (b)

Figure 8.8: SHG response from Sample *J* with ≈290 nm wide silicon wires constituting a grating with a 600nm period.

incoming electrical field was also obtained for Sample *J*. The response is seen in Figure 8.8. It is seen that the response at 0 degrees and 180 degrees found in Figure 8.7 now seems to be found at 90 degrees and 270 degrees which also would be expected from the change in polarisation.
To further investigate if the grating periodicity has an impact on the second harmonic response, the linear response is measured. For this purpose a photo diode was introduced into the experimental setup—right after the sample holder. The linear responses for both Sample F and J are shown in Figure 8.9. For both gratings the characteristic angles seen from the second harmonic responses are once again prominent. This amplifies the assumption that the observed responses at these angles are related to the distinct periodicity of the gratings. The explanation for the observed second harmonic response may be found from the grating equation:

$$a(\sin(\theta_{out,m}) + \sin(\theta_{in})) = m\lambda, \tag{8.1}$$

where a is the grating period, and $m = (0, \pm 1, \pm 2, ...)$. The diffracted angles as a function of the rotated angle are shown in Figure 8.10. It is seen that for $m = \pm 2$,

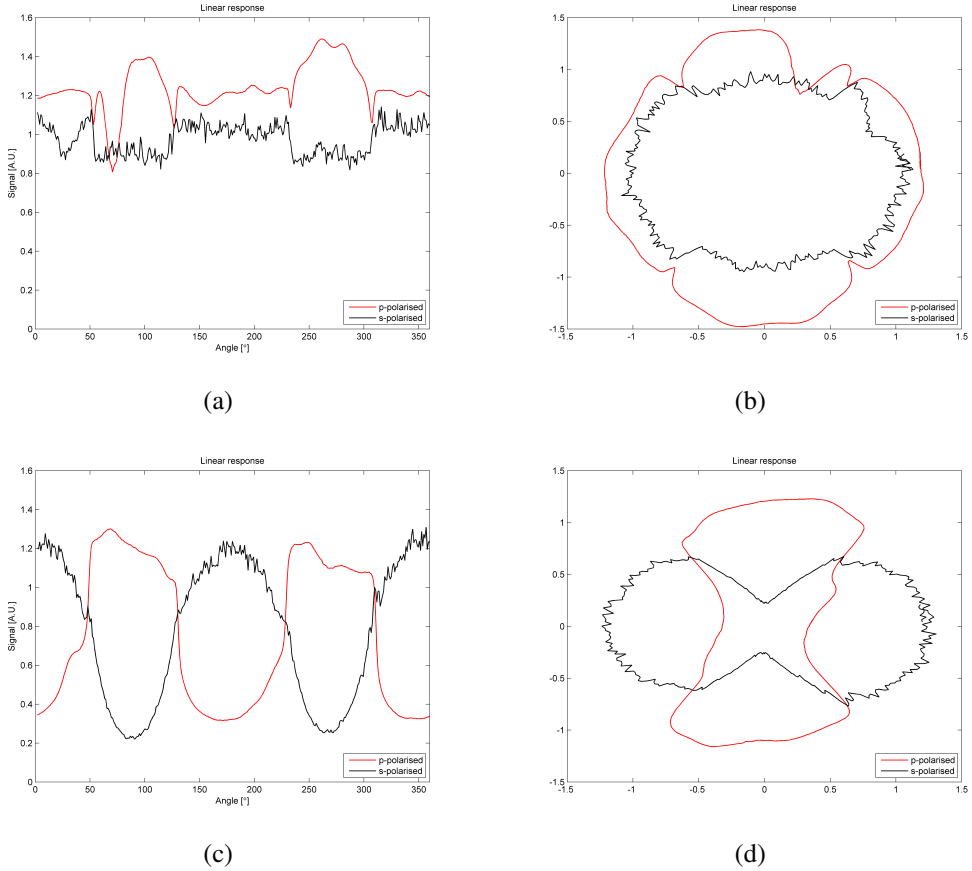

Figure 8.9: (a) and (b) Linear response from Sample *F*. (c) and (d) Linear response from Sample *J*.

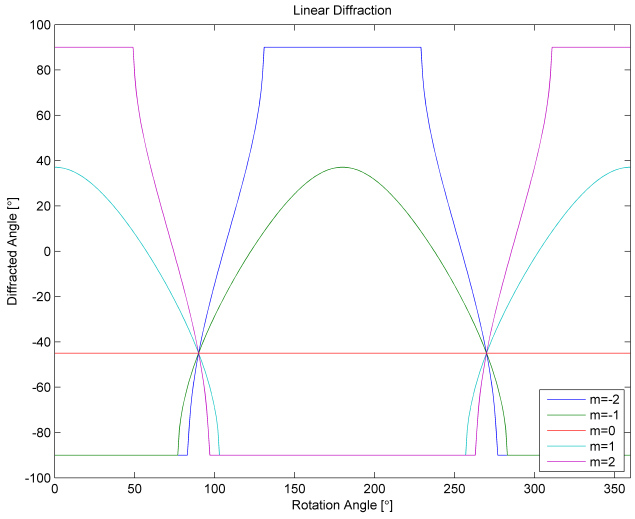

Figure 8.10: The first orders of diffracted angles as a function of the rotated angle. The grating period is 600 nm, the wavelength is 786 nm and the angle of incidence is 45 degrees.

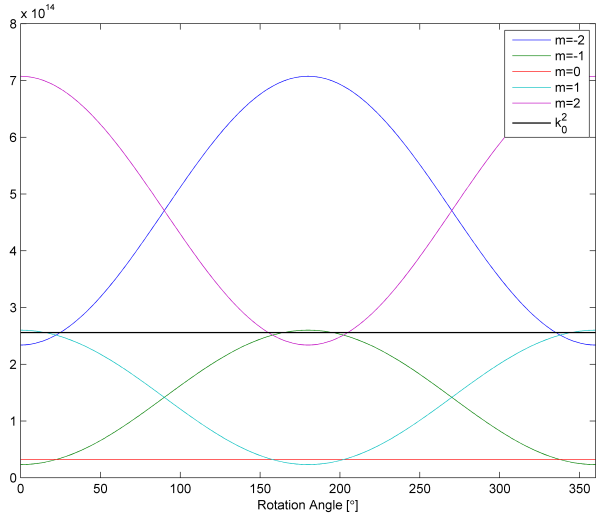

Figure 8.11: Second harmonic diffraction condition for the first few orders as a function of the rotated angle. The grating period is 600 nm, the wavelength is 786 nm and the angle of incidence is 45 degrees.

the diffraction lies in the plane of the grating (diffracted angle=90 degrees) at the specific angles observed in the spectra for both the linear and second harmonic responses. The increase in second harmonic response at these angles can thus be due to further enhanced near-fields due to the linear diffracted orders. The diffracted $m = \pm 2$ orders also diffract at -90 degrees at some angles of the rotation, however, these angles do not show up in the measured spectra as particularly important.
Another explanation could be found in the diffraction condition for the second harmonic response. The pumping wave vector can be written as $\vec{k}_{in} = k_0^{\omega}(\hat{x}\sin(\alpha) - \hat{z}\cos(\alpha))$ where α is the angle of incidence. The diffracted second harmonic wave vector can then be written $\vec{k}_{out} = k_0^{\omega}\hat{x}\sin(\alpha) + m\vec{G} + \hat{z}f_{m,\alpha}$ where f is some value that depends on the angle of incidence and the diffracted order. $\vec{G} = \frac{2\pi}{a}(\hat{x}\cos(\theta) + \hat{y}\sin(\theta))$ is the vector describing the reciprocal grating, where a is the grating period and θ is the rotated angle. The diffraction condition thus become:

$$\begin{aligned} |\hat{x}k_0^{\omega}\sin(\alpha) + m\frac{2\pi}{a}(\hat{x}\cos(\theta) + \hat{y}\sin(\theta))| &< k_0^{2\omega} \Rightarrow \\ (k_0^{\omega}\sin(\alpha) + m\frac{2\pi}{a}\cos(\theta))^2 + (m\frac{2\pi}{a}\sin(\theta))^2 &< (k_0^{2\omega})^2 \end{aligned} \tag{8.2}$$

Solving this for the first few orders yield the result seen in Figure 8.11. It is seen that the condition for diffraction goes from being fulfilled to not being fulfilled at angles not corresponding to those instances where the strong responses are observed in the second harmonic spectra. It thus seem that the first outlined mechanism is the most plausible.

Second harmonic measurements on the 1 mm$\times$1 mm area samples are shown in Figures 8.12 to 8.19. During the rotation, the p-polarised laser beam could not be kept wholly within the grating area. Three measurements were done on each

sample and in between each measurement the sample was reorientated in an attempt to improve the result.

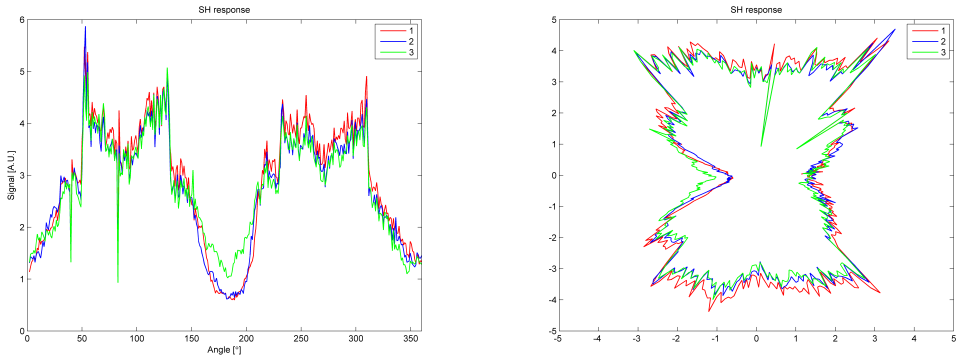

(a) (b)

Figure 8.12: SHG response from Sample *A* with ≈340 nm wide gold wires constituting a grating with a 600 nm period.

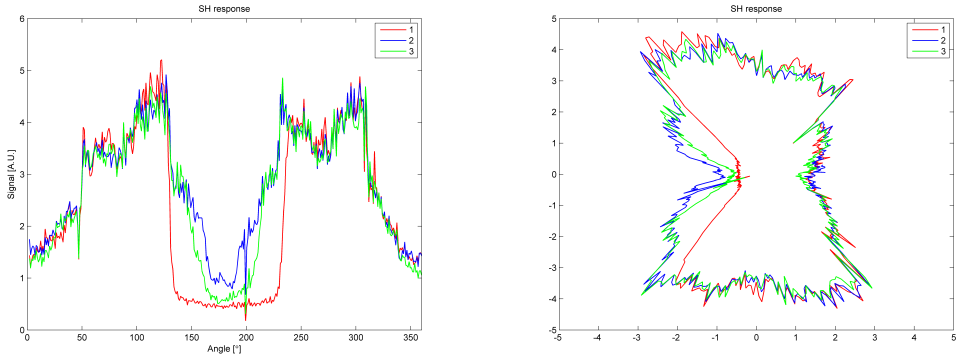

(a) (b)

Figure 8.13: SHG response from Sample *B* with ≈350 nm wide gold wires constituting a grating with a 600 nm period.

Taking into account that the gratings were not illuminated evenly during the 360 degrees rotation, qualitatively, the spectra resemble those from Samples *F* and *J*. The wire width has been increased for the gold gratings from Sample *A* to *E*. No clear dependence of wire width on the second harmonic response is observed. From the modelled near-fields in Chapter 5, it was found that an increase in field enhancement between the wires could be expected with increasing wire width while the grating period was kept constant. One could thus expect an increase in response from Sample *A* to Sample *E*. In fact, a small increase is observed but due to the uncertainty of how well the exciting field was focused on the gratings, this connection cannot be solidified.

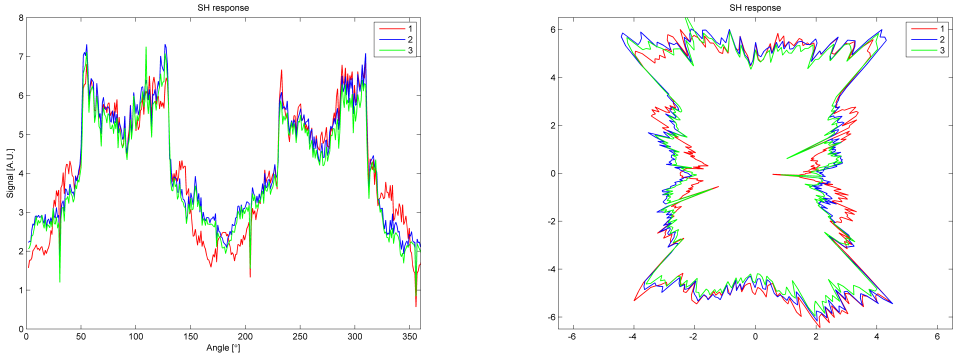

(a) (b)

Figure 8.14: SHG response from Sample *C* with ≈355 nm wide gold wires constituting a grating with a 600 nm period.

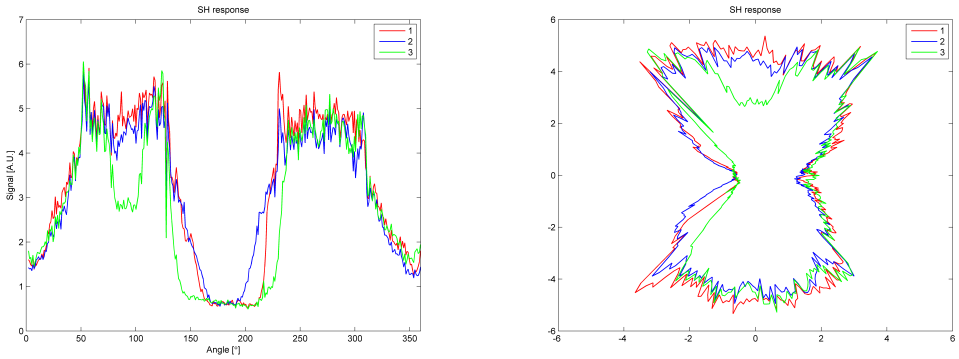

(a) (b)

Figure 8.15: SHG response from Sample *D* with ≈375 nm wide gold wires constituting a grating with a 600 nm period.

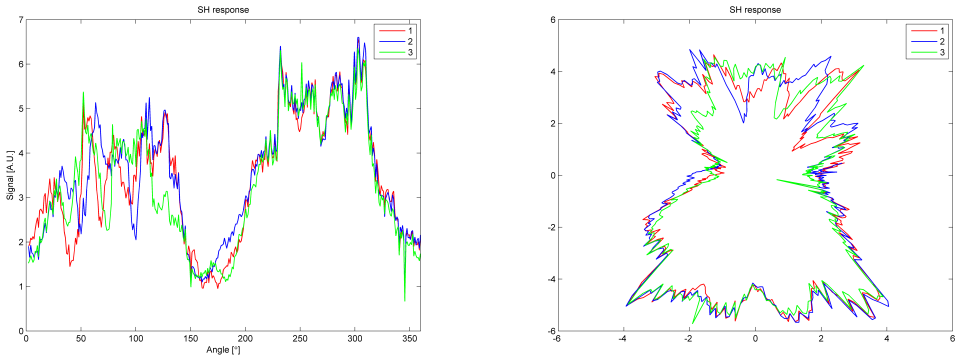

(a) (b)

Figure 8.16: SHG response from Sample *E* with ≈390 nm wide gold wires constituting a grating with a 600 nm period.

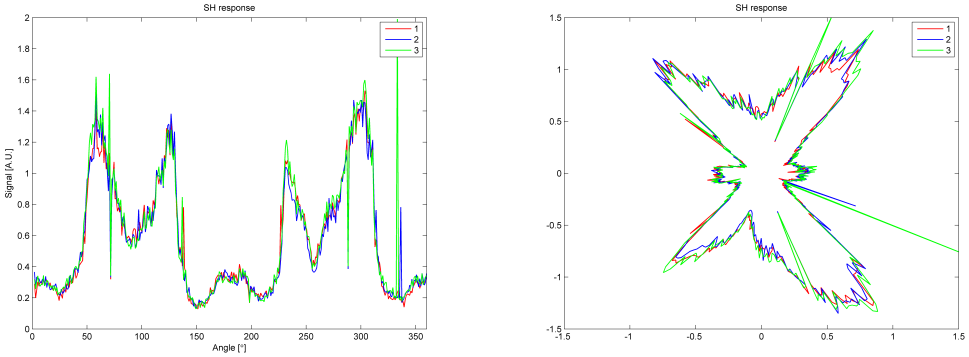

(a) (b)

Figure 8.17: SHG response from Sample *G* with ≈210 nm wide silicon wires constituting a grating with a 600 nm period.

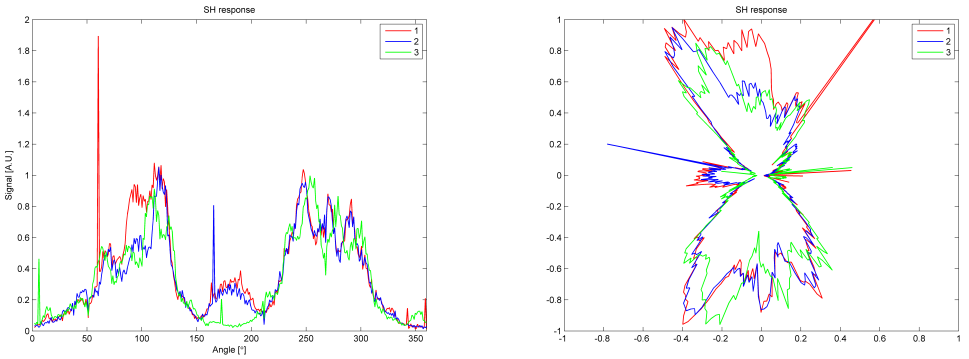

(a) (b)

Figure 8.18: SHG response from Sample *H* with ≈270 nm wide silicon wires constituting a grating with a 600 nm period.

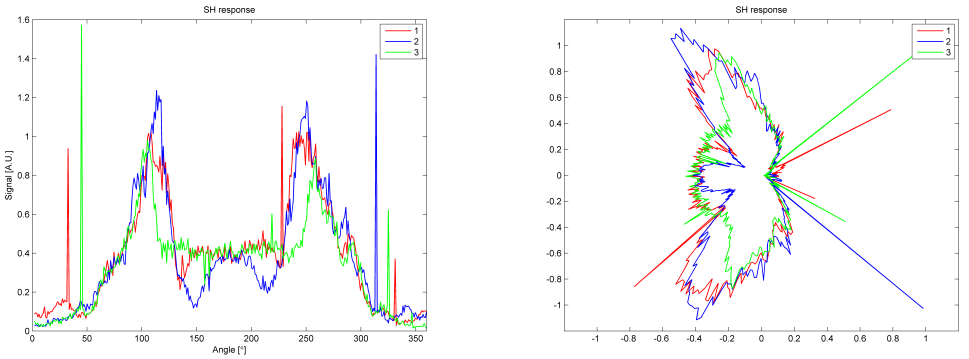

(a) (b)

Figure 8.19: SHG response from Sample *I* with ≈320 nm wide silicon wires constituting a grating with a 600 nm period.

Conclusion

III

In this part, a conclusion is found which sums up what was done and investigated during the project.
In the end, a chapter is located which suggests further possible actions to learn more about the optical nature of metallic gratings and their making.

Conclusion 9

Two types of plasmons exist—namely surface plasmon polaritons and localised surface plasmons. Both types of plasmons are collective oscillations of electrons due to an exciting electromagnetic field. The surface plasmon polariton is the excitation of electrons in the surface of a metal with a surrounding dielectric. The forming of a surface plasmon polariton requires an electromagnetic field incident on the surface such that both a perpendicular and in-plane wave vector component is present. The surface plasmon polariton is free to move along the surface but is confined perpendicular to the surface-plane. The plasmon decays exponentially into both the metal and the dielectric. Through modelling it was found that if the waveguide is made of gold, the penetration depth of the plasmon into the gold surface is in the range of $\approx$20 nm. In order to excite a surface plasmon polariton, a momentum component is needed to be added to the in-plane wave vector component of the exciting field. This wave vector component can originate from enhanced near-fields or from periodic scatterers like e.g. a grating. Localised surface plasmons are locally confined to metallic nanostructures, where the resonance condition of the plasmon arises naturally as a consequence of metal-type and dimensions of the nanostructure i.e. confinement of the electrons is required. Resonance conditions can be found analytically for very small nanoparticles with cylindrical geometry. Larger particles and arbitrary shaped structures requires that Maxwell's equations are solved for the problem.
Through use of Green's function, Maxwell's equations are solved for a gold grating where the electrical field is oriented along the wire-axis of the grating. With this polarisation of the electrical field, the plasmon resonance condition could not be fulfilled since no confinement of the electrons along the electrical field was possible. Still, a change in near-field intensity was observed between the wires. Within the visible regime, it was found that the intensity of this near-field increased with the wavelength of the exciting field—furthermore, the placement of the near-field moved farther away from the surface of the wires. The near-fields were situated within a couple of hundreds nm's from the grating surface. Also, a variation of the wire widths was done. For increasing wire width, the same phenomenon as for an increase in wavelength was observed. Again the intensity of the near-fields increased and the placement of the field moved away from the grating.

Gold and silicon gratings were produced through e-beam lithography. The lithography process was problematic. Different initiatives were taken towards resolving the problem and in the end—more or less successful gratings were produced. The silicon gratings were etched from plain silicon wafers. The gold gratings were made by evaporating gold onto silicon wafers with lithographically written struc-

tures and subsequently performing lift-off. Gratings with different wire widths were made and these were characterised by scanning electron microscopy. All gratings were with a 600 nm period and the widths of the gold wires ranged from ≈325 nm to ≈390 nm while the height through atomic force microscopy was found to be ≈60 nm to ≈65 nm.

The theory of second harmonic generation relates the second harmonic response particularly to surfaces where the inversion symmetry is broken and to strongly enhanced electrical fields. This optical characterisation method was thus chosen as an indirect way of possibly identifying plasmon resonances in connection with the produced gratings. No unambiguous signs of excited plasmon resonances was found. The observed responses—and change in responses—was accredited to mainly changes in the effective second order susceptibility due to the structure of the grating. Also, diffraction from the gratings were believed to be of dominant importance. This was further solidified by linear measurements and theoretical modelling. It is believed that the theoretical dependence of wire width on near-field intensity for an *s*-polarised field can be transferred to the *p*-polarised situation. This dependence was sought verified by second harmonic measurements, but again no unambiguous relation could be established—primarily due to the quality of the measured second harmonic spectra.

10 Perspectives

It could be interesting to investigate the response of the produced gratings at a rotated angle of 0 degrees and 90 degrees for a continuum of pumping wavelengths. Also, it would make sense to produce additional gratings with altered periodicity in order to solidify that the effects believed to originate from diffraction conditions are in fact valid. A more direct way of investigating the near-fields of the gratings would be to perform near-field microscopy on them.

The near-field modelling in Chapter 5 was done without the silicon background and only for *s*-polarised excitation. Future modelling could involve the excitation with a *p*-polarised field in order to investigate if any plasmon resonance conditions are being fulfilled. It was mentioned that the memory requirements for the written program were quite high and a solution to this could be to use commercialised modelling software like e.g. COMSOL. COMSOL also offer the possibility of invoking periodic boundary conditions in the model and so the model can be made with only a single wire. Another interesting project could be to model wires with a triangular cross section—these geometries are known to have strongly enhanced near-fields at the corners.

Also, gratings of wires with triangular cross sections could be produced and investigated with respect to their optical properties. This could e.g. be done through ion-milling where a gold surface is subjected to writing by a focused ion beam. Through a lithographic process, it is rather cumbersome to make triangular wires. One possible way of attaining the desired wires would be to produce a grating mask as done in the present project—but on a silicon on insulator (SOI) wafer. Next, the sample is subjected to reactive ion etching—using much the same settings as described in Section 7.5, but leaving out the oxygen flow. The silicon is more readily etched than the silicon dioxide and etching the sample for a prolonged period of time will create a cavity beneath the PMMA mask (cf. Figure 10.1). The reason

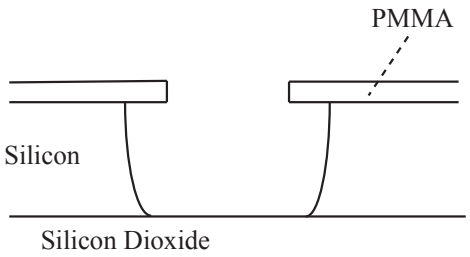

Figure 10.1: Formed cavity due to prolonged etching.

for leaving out the oxygen flow is that the PMMA is not etched away as fast as if

the oxygen was present. Following this, gold is sputtered onto the sample which gradually closes the mask holes and letting smaller and smaller amounts of gold reaching the insulator layer. Finally the remaining silicon on top of the insulator and the PMMA mask can be removed through etching and the wanted structure has been finished. Another possible way of attaining the triangular cross sections is to follow the approach as outlined by [1].

Bibliography

[1] Alexandra Boltasseva, Velentyn S. Volkov, Rasmus B. Nielsen, Esteban Moreno, Sergio G. Rodrigo, and Sergey I. Bozhevolnyi. *Triangular metal wedges for subwavelength plasmon-polariton guiding at telecom wavelengths*. Optical Express, 16, No. 8, 2008.

[2] Robert W. Boyd. *Nonlinear Optics*. Academic Press, Inc., 1992. ISBN 0-12-121680-2.

[3] Zheng Cui. *Nanofabrication - Principles, Capabilities and Limits*. Springer, 2002. ISBN 978-0-387-75576-2.

[4] W. Daum. *Optical studies of Si/SiO_2 interfaces by second-harmonic generation spectroscopy of silicon interband transitions*. Applied Physics A, 87, 2007.

[5] Jens Christian Uggerhøj. *Manufacturing Silicon Field Effect Transistors - for Sensor Applications*. 8th semester project, 2010.

[6] Jesper Jung. *Solar Cell Physics and Technology, PhD Course*. Lecture Material, 2011.

[7] A. V. Krasavin and A. V. Zayats. *All-optical active components for dielectric-loaded plasmonic waveguides*. Optics Communications, 283, 2010.

[8] A. V. Krasavin and A. V. Zayats. *Electro-optic switching element fir dielectric-loaded surface plasmon polariton waveguides*. Applied Physics Letters, 97, 2010.

[9] Kevin F. MacDonald and Nikolay I. Zheludev. *Active plasmonics: current status*. Laser & Photon. Rev., 2009.

[10] Stefan Alexander Maier. *Plasmonics - Fundamentals and Applications*. Springer, 2007. ISBN 978-0387-33150-8.

[11] Lukas Novotny and Bert Hecht. *Principles of Nano-Optics*. Cambridge, 2006. ISBN 978-0-521-83224-3.

[12] E. D. Palik. *Handbook of Optical Constants of Solids*. Academic Press Inc., 1985. ISBN 0-12-544420-6.

[13] Peder Jørgensgaard Olesen, Peter Sommer-Larsen, Jens Christian Uggerhøj. *Surface Probing using Second Harmonic Generation*. 6th semester project, 2008.

[14] Thomas G. Pedersen, Jesper Jung, Thomas Søndergaard, and Kjeld Pedersen. *Nanoparticle plasmon resonances in the near-static limit*. Optics Letters, 36, No. 5, 2011.

[15] G. Schider, J. R. Krenn, W. Gotschy, B. Lamprecht, H. Ditlbacher, A. Leitner, and F. R. Aussenegg. *Optical properties of Ag and Au nanowire gratings*. Journal of Applied Physics, 90, No. 8, 2001.

[16] Thomas Søndergaard. *Nano optics - Integral method based on Green's function (2D)*. Note, 2010.